CHALMERS

Analyzing the Mechanical Behavior of Additive Manufactured Ti-6Al-4V Using Digital Image Correlation

Diploma work in the Master programme Materials Engineering

ALEXANDER LEICHT
ELON OSKAR WENNBERG

Diploma work No. 157/2015
Department of Materials and Manufacturing Technology
CHALMERS UNIVERSITY OF TECHNOLOGY
Gothenburg, Sweden 2015

Analyzing the Mechanical Behavior of Additive Manufactured Ti-6Al-4V Using Digital Image Correlation

Alexander Leicht
Elon Oskar Wennberg

Diploma work No. 157/2015
at Department of Materials and Manufacturing Technology
CHALMERS UNIVERSITY OF TECHNOLOGY
Gothenburg, Sweden

Diploma work in the Master programme Materials Engineering

Performed at: SP Technical Research Institute of Sweden / Chalmers University of Technology

Supervisor: Torsten Sjögren
SP Technical Research Institute of Sweden,
Brinellgatan 4, 504 62 BORÅS

Examiner: Johan Ahlström
Department of Materials and Manufacturing Technology
Chalmers University of Technology, SE - 412 96
Gothenburg

Analyzing the Mechanical Behavior of Additive Manufactured Ti-6Al-4V Using Digital Image Correlation
Alexander Leicht
Elon Oskar Wennberg

Diploma work no 157/2015
Department of Materials and Manufacturing Technology
Chalmers University of Technology
SE-412 96 Gothenburg
Sweden
Telephone + 46 (0)31-772 1000

Chalmers University of Technology
Gothenburg, Sweden 2015

Summary

Demands from the market to produce high performance products with low lead times and more customized production are continuously increasing. This has resulted in a growing market for additively manufactured components. Two printing techniques, selective laser melting (SLM) and electron beam melting (EBM), were compared by investigating their resulting mechanical performance. Samples manufactured from Ti-6Al-4V powder were provided from Arcam AB and Lasertech LSH AB. Both companies made two different build layer orientations, one set was built parallel to the tensile direction (X) and another perpendicular to the tensile direction (Z). Half of the samples produced with SLM were heat treated.

Samples were tested under quasi-static tensile loading in combination with Digital Image Correlation (DIC) to determine the localized strains. From each tensile test, Young's modulus, yield strength ($R_{p0.2}$), ultimate tensile strength (UTS) and elongation at break were obtained. A Vickers hardness test (HV2) was performed on polished surfaces. Optical microscope was used in order to analyze the microstructure of the samples.

For all samples it was seen that the grains have grown in an epitaxial manner in the same direction as the building direction. An explanation for this was the re-melting of layers. Results from the DIC analysis indicate that the X-built EBM and SLM samples contain localized strains elongated perpendicular to the tensile direction and potentially connect to the areas of the prior β-grains. The Z-built EBM and SLM samples seem to have localized strains elongated in the tensile direction. By comparing the strain fields of the SLM samples it can generally be noted that the strain fields are more homogeneous in the Z-built samples. From the mechanical tests it was shown that different mechanical properties are obtained in samples from the different manufacturing processes.

Keywords

Additive manufacturing, Digital image correlation, DIC, Electron beam melting, Mechanical characterization, Selective laser melting, Strain fields, Ti-6Al-4V

Acknowledgements

For all the help and guidance during this thesis work we would like to express a special thanks to our supervisor Torsten Sjögren at SP Technical Research Institute of Sweden. We would also like to thank our examiner Johan Ahlström at Chalmers University of Technology.

Contents

1. Introduction

Demands from the market to produce high performance products with low lead times and more customized production are increasing every day. This has stimulated the development of new manufacturing techniques. One upcoming technique is the use of additive manufacturing (AM) to create dense complex metal components. However, there are gaps in the understanding of how these AM built materials behave in practice and also a need to verify their mechanical performance.

SP Technical Research Institute of Sweden is involved in a project where the aim is to optimize the production process for AM in metal and especially the alloy Ti-6Al-4V. An initial step in that project is this thesis work.

1.1. Purpose and research questions

One objective of this study is to examine if there is any obvious difference in mechanical performance between materials manufactured by Selective Laser Melting (SLM) or Electron Beam Melting (EBM). Additive manufactured Ti-6Al-4V alloy will be tested under static tensile loading in combination with Digital Image Correlation (DIC) analysis. It is of interest to investigate if the building direction will have an effect on mechanical performance and to see if any inhomogeneities can be observed in the strain fields from the DIC analysis. It is also of interest to study how the material fails with respect to the microstructure and the layer dependency, created through the layer-by-layer production methodology. With this motivation the following research questions are to be identified:

1. Is there any obvious difference in mechanical performance depending on the building process?

2. Is there any obvious difference in mechanical performance depending on the layer orientation?

3. Is there any inhomogeneous strain fields that can be connected to the microstructure and building direction of additive manufactured Ti-6Al-4V?

1.2. Delimitations

Since the additively manufactured samples are provided from a third part and the material is fixed to Ti-6Al-4V, it is assumed that the material specification conforms to the ASTM F2924 standard. Samples will be tested as-delivered, with the exception of final machining of the samples. No other AM processes than SLM and EBM will be analyzed. This work will not cover fatigue testing, only quasi-static conditions.

1.3. Outline and Method

The project will start with a literature survey which will include general information about the Ti-6Al-4V material. The analysis tools (DIC and optical microscope) and the printing techniques (SLM and EBM) will be explained. The printing techniques will be compared to find differences concerning mechanical performance of their final products.

The next step of the project will be experimental characterized of additively manufactured samples. For the DIC analysis the delivered test pieces will be polished on one side followed by etching. The other side will be painted with white color followed by spraying of a unique black pattern. The software utilizing DIC will gather information in form of images during the tensile tests. The macroscopic deformation pattern will be gathered from the painted side of the sample monitored with a CCD camera, and the microscopic deformation pattern of the samples is gathered from a digital microscope aimed at the polished and etched side of the sample. Hardness tests will be performed to gather information about the different samples. The final step will be to analyze the test data, correlate all the parameters and to relate it to results from the literature.

2. Literature Survey

This section includes background information from previous work, information concerning material and manufacturing processes.

2.1. General about Titanium

Today titanium alloys are used in a wide range of applications. Titanium alloys have a high price but their properties could make them competitive in certain applications. Two fast growing markets for titanium are aerospace and medical implant industry with products like turbine blades and hip-implants. The major benefits of titanium alloys are their high specific strength and biocompatibility. Titanium alloys are very reactive, especially with oxygen, which results in the formation of a corrosion resistant oxide layer on the alloy surface. Due to the reactive nature of titanium alloys, the atmosphere during high temperature processing needs to be vacuum or inert gas, otherwise the material could become contaminated. High strength in combination with low thermal conductivity makes the material difficult to machine [1].

In the mid-50s a titanium alloy called Ti-6Al-4V made a big breakthrough due to its excellent combination of mechanical and manufacturing properties. Compared to commercially pure titanium the Ti-6Al-4V has higher strength and fatigue resistance. Ti-6Al-4V is a dual-phase α+β material which means that the equilibrium microstructure is a fine mix of the both phases [1].

Ti-6Al-4V behaves differently and develops different microstructure depending on its time-temperature history. In order to realize how Ti-6Al-4V behaves with varying cooling rates, it is of interest to know how its alloying elements affect the material. Aluminum is an α-phase (HCP) stabilizer and vanadium is a β-phase (BCC) stabilizer. By increasing the content of vanadium the β-phase is stable at lower temperatures, see Figure 1. With increasing content of aluminum the α-phase will be stable at higher temperatures [1].

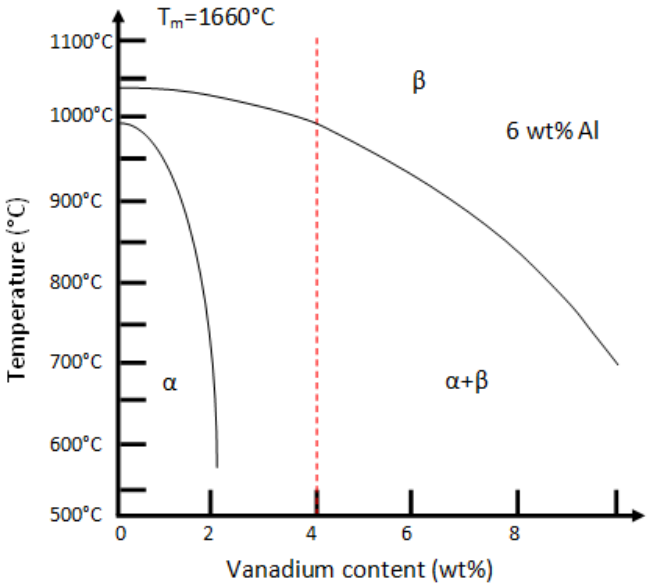

Figure 1 - Schematic phase diagram of Ti-6Al-4V presenting the phase regions α, α+β and β as a function of vanadium content and/or temperature, based on [1].

Oxygen, iron and other elements are impurities which could impair the mechanical properties in titanium alloys. According to ATSM F2924 standard for additive manufactured Ti-6Al-4V the composition should be according to Table 1 [2].

Table 1 – ASTM F2924 standard composition of additive manufactured Ti-6Al-4V with powder bed fusion.

Element (wt. %)	Ti	N	C	H	Fe	O	Al	V
ASTM F2924	Bal.	< 0.05	< 0.1	< 0.015	< 0.3	< 0.2	5.5-6.75	3.5-4.5

The equilibrium microstructure of Ti-6Al-4V at room temperature is a combination of both α- and β-phase. The α-phase is the larger fraction in equilibrium state, however some retained β-phase is present. The different microstructures and micro constituents present at room temperature are highly dependent on the cooling rate and previous heat treatments of the alloy. When the cooling rate is slow and starts from temperatures close to, or above, the β-transition temperature (approximately 995°C), β-phase will start transforming into primary α-phase as the temperature drops. Slow cooling results in β-grains including an α-phase [1, 3].

If the cooling rate is increased the nucleation rate of α-phase on the β-grain boundaries will increase. This increase leads to an increase of α-platelets grown into the β-grains. However, with increased cooling rate the diffusion process for α-phase is decreased. Higher cooling rates thus yields thinner additional α-platelets. The width and length of α-platelets can thus be tailored with cooling rate. Further increase of the cooling rate results in even higher nucleation rate of α-phase. At high cooling rates α-phase nucleation sites can be found inside the β-phase matrix. Generally an increased cooling rate leads to more lamellar microstructure [1, 3].

Very high cooling rates results in formation of a fully or partially martensitic α-structure from the prior β-phase. The martensitic structure can take form of α'- or α"-martensite. The quantity of each martensitic structure is highly dependent on the solution treatment temperature of the alloy prior to cooling. The final microstructure at room temperature then takes form of a basket-weave structure [3].

Titanium for additive manufacturing (AM) is often supplied in form of a powder with a diameter between 25-105 μm. Powders can be manufactured by different manufacturing methods. Most common is the gas atomization process, where a gas stream breaks the molten metal to create droplets. Since titanium is highly reactive this process needs to be performed in a noble gas environment, like argon. Other atomization processes are chemical electrolytic or mechanical [4].

2.2. Additive manufacturing

Additive manufacturing (AM) is also referred to as 3D-printing, freeform fabrication, rapid manufacturing and rapid prototyping. The freedom of design that opens up when using AM allows for creation of designs impossible or very costly to manufacture with conventional manufacturing methods [4].

Through additive manufacturing dense components with near-net shape are possible to produce. In the last two decades AM has developed to include several material classes e.g. ceramics, polymers and metals [4]. Most metallic components are built from a pre-alloyed powder, manufactured either by an Electron Beam Melting (EBM) or Selective Laser Melting (SLM) process. The final geometry of the components is defined by a 3D-CAD model [5].

The most common AM principle for metals is powder bed fusion which is a layer-by-layer based process, utilized in both EBM and SLM. The process starts with a CAD file where the design is split up into thin cross-sections of specified thickness. The powder is added from powder hoppers onto a building plate by the use of a rake, see Figure 2. One passing with the rake supplies powder for one layer in the CAD model. The added powder correlates to a specific cross-section or layer in the CAD model. After each rake passing, powder is fused/melted together in the pattern specified from the cross-section in the CAD model. To control the thickness of the building layers the machine lowers the build plate a specified distance following each melting process [5].

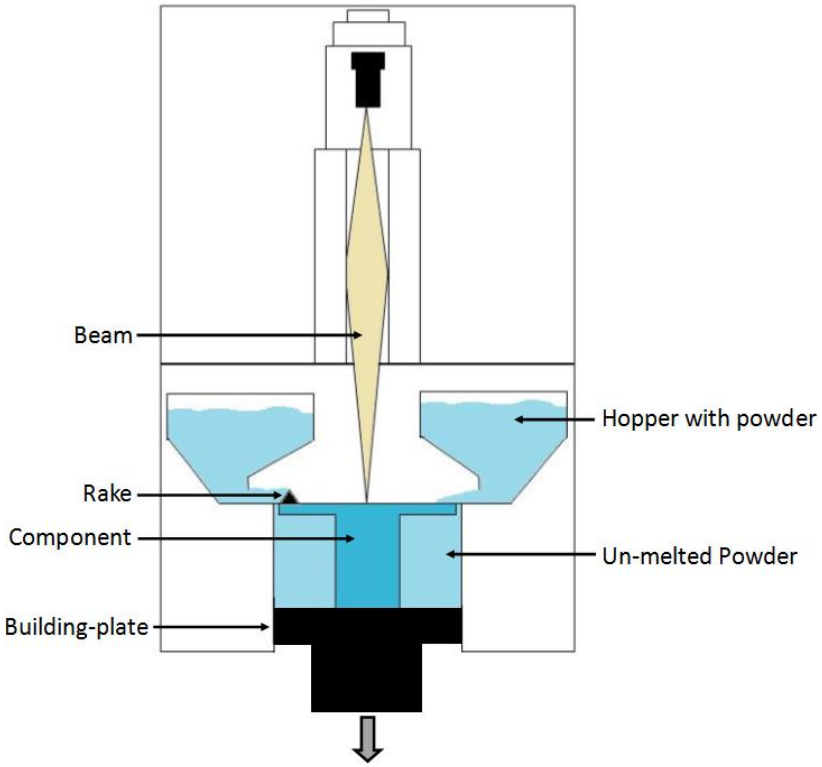

Figure 2 – Schematic design for layer-by-layer based AM processes.

The process for AM in metals is not limited to layer-by-layer based printing. Direct printing, where molten metal droplets continuously build a product, does exist [6].

For layer-by-layer based processes, supporting structures are needed during the build. They can be automatically placed in the CAD model with a pre-processing software. However, their placements are usually over compensated to make sure the built structure is rigid. Not to waste material and increase the post-processing, the supports should be designed for easy removal [6].

2.2.1. Selective laser melting (SLM) and Electron beam melting (EBM)

Selective laser melting uses a laser beam to melt the powder material. The laser beams are usually formed from a CO_2 or Nd:YAG source, where Nd:YAG stands for yttrium aluminum garnet doped with neodymium [7]. SLM machines have laser sources of very high beam quality [8]. The basic principle for SLM starts with the laser source. Light is guided from the source and is focused through a laser head onto the powder bed of the machine. The laser head can be moved in two directions in a plane parallel to the powder bed, or the beams can be guided by movable mirrors. To minimize contamination and oxidation of the built material the build chamber is often flushed with argon or another noble gas of choice. The complete SLM build process is run at room temperature, where the laser heats and melts only the powder according to the present layer layout [5, 8].

EBM is using a high energy electron beam in order to melt the powder and this process is performed in vacuum at high temperature. Vacuum is required as the electrons will scatter on atoms in gaseous environments [4]. Vacuum contributes to less oxidation and slower cooling rates [5]. The electron beams in the EBM machine are controlled with electromagnetic coils. Through the rapid movement of the electron beam by these coils the EBM process is able to maintain several melt pools in parallel [9].

Some studies state that the use of vacuum in EBM allows for less thermal distortion, leaving the finished product with overall better properties and faster build time than if built with SLM [6]. Also, other studies state that SLM has higher strength and lower ductility than EBM [5]. In SLM there is a large temperature gradient during the building process which results in thermal stresses which can be relieved in a post processing heat treatment [10]. A drawback of EBM is that it could give worse surface properties, to be further explained in section 2.3. On the other hand an SLM process can give worse dimensional stability [5, 6].

2.2.2. Microstructure of additive manufactured Ti-6Al-4V

Additive manufactured components have a complex thermal history and the microstructure will depend on the process and which parameters that have been used. Mechanical properties will depend on chemical composition, heat treatment and processing history. In general additive manufactured Ti-6Al-4V parts have much finer microstructure than a wrought Ti-6Al-4V component. The fine microstructure can be seen in Figure 3. There are differences in thermal history between EBM and SLM thus, as-built, they will have different microstructure and mechanical properties [10, 11].

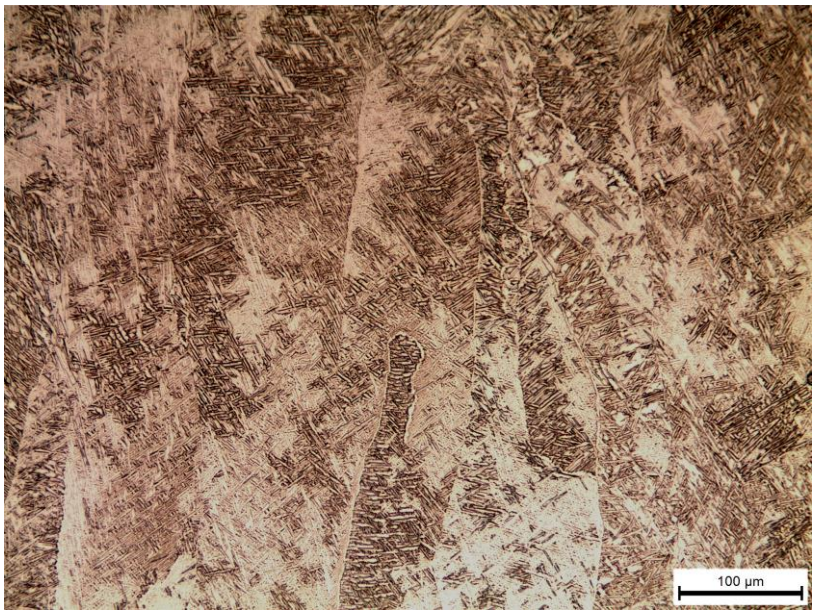

Figure 3 – Microstructure of an EBM produced Ti-6Al-4V sample.

In the EBM process, each powder layer is preheated with an unfocused electron beam to around 700°C. The component retains this temperature throughout the building process. After preheating the top layer, a focused electron beam will melt the top layer and also partly re-melt the layer below merging them together at a temperature of 1900°C. Solidification occurs rapidly from melt to solid with a cooling rate of 10^3-10^5°C/s. The temperature stagnates at the preheated temperature in the build chamber. When the building process is done the temperature decreases slowly from 700°C to room temperature [10, 11].

The SLM process has no preheating of the powder prior to melting. The top layer is melted with a laser beam and merged with the layer below approximately at the same temperature as for EBM. This process has comparable cooling rate to EBM (10^3-10^5°C/s) but the temperature returns soon to room temperature instead [11].

Generally during solidification of Ti-6Al-4V the melt completely transforms to β-phase when passing the solidus line. The β-grains formed initially are known as prior β-grains. For both EBM and SLM processes the cooling rate is high enough to enable α'-phase (acicular martensitic structure) transformation. The required cooling rate for α'-formation is 420°C/s [10, 11].

Cooling in the EBM process stagnates at the preheating temperature which is in the α+β region, see Figure 4. Parts produced from this method undergo an in-process thermal treatment comparable to tempering. This result in that the α'-phase inside the prior β-grains transforms to a α+β-phase. The α-phase will grow inside the prior β-grains normal to the grain boundary, see Figure 5. Full transformation takes around 30 minutes depending on temperature and component size, this time is usually much shorter than the total building time for EBM. If any retained β-phase was formed during cooling it will transform to α+β-phase as well [11].

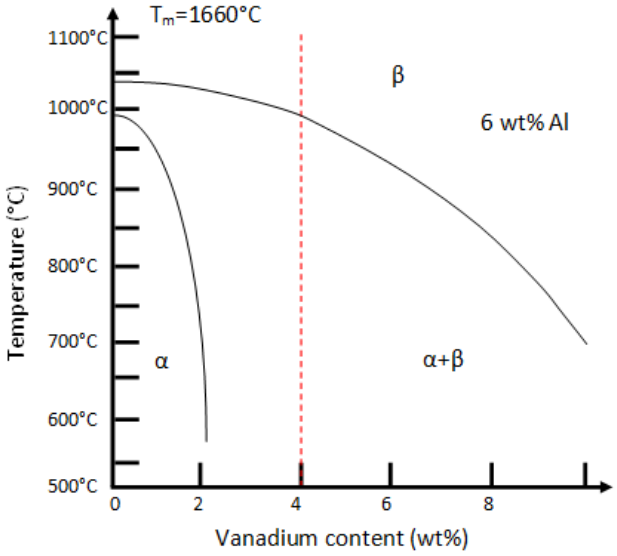

Figure 4 – Schematic phase diagram of Ti-6Al-4V, based on [1].

The SLM process on the other hand includes no preheating and the final microstructure will thus consist of α'-phase with some retained β-phase. Depending on the application SLM parts might need separate heat treatment to transform the α'-phase into the more ductile α+β-phase [10].

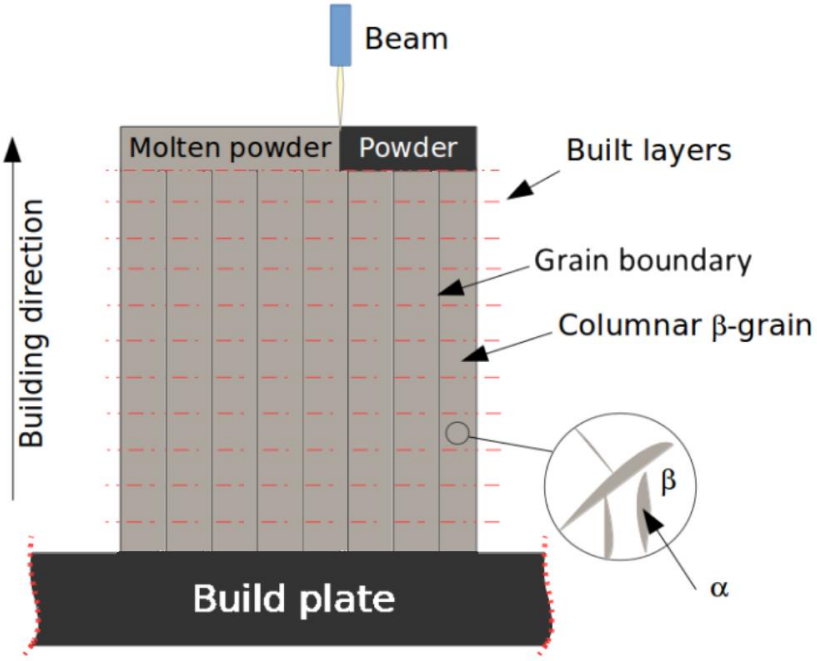

Figure 5 - Illustration of columnar growth of prior β-grains, with α-phase inside the β-grains.

When passing the liquidus line in both SLM and EBM processes the growth of prior β-grains occur very quickly and these will grow in a columnar manner in the same direction as the building direction, see Figure 5. The beam in each process forms a melt pool from which heat is conducted to the surrounding and to the already built layers. Since the material below the top layer will be partly re-melted, the grains grow epitaxially from the layer below. This results in that those grains will span over several layer widths, shown in Figure 5. It is assumed that the growth direction follows the temperature gradient. Looking closer to the surface of parts the growth direction can deviate from the building direction since the temperature gradient is different. It has not been seen that the α-phase follow any specific growth direction [11].

2.2.3. Mechanical properties of Ti-6Al-4V

As for all metals the microstructure has a large impact on the final properties in components. When comparing Ti-6Al-4V manufactured either by SLM or EBM a major difference is the cooling rate. This will affect the microstructure and thereby the final mechanical properties. Favorable properties will depend on application requirements [12].

As-built SLM materials will have a martensitic structure resulting in a higher tensile strength but also a lower ductility in comparison with EBM materials which will have a α+β structure. It has been shown that the martensitic transformation mainly depends on the cooling rate and is not critically affected by slight variances in alloy composition [12]. The high cooling rate of as-built SLM components results in development of residual stresses which could have an effect on the distortion of produced components. In order to increase the ductility and limit the distortion of these components they can be stress-relieved. This process will transform the martensitic structure into α+β phase [13].

Tensile strength of EBM samples have been shown to relate to the width of the α-laths, coarser α-lath will reduce the tensile strength, meaning that a slight increase of temperature in the building chamber can reduce the tensile strength drastically. As for many materials the yield strength and hardness relates to the grain size. For Ti-6Al-4V, the size of the prior β-grains will determine how some mechanical properties will change. According to Hall-Petch relation: $\sigma_y = \sigma_0 + \frac{K}{\sqrt{D}}$, were σ_0 is the single crystal yield strength, K is a material constant and D is the grain diameter, the yield strength (σ_y) will decrease with an increase of grain size. Dislocation density and inclusions are other factors that can have an impact on yield strength [12, 14].

The pores in AM components are categorized into two groups, elongated or spherical. The elongated pores might evolve due to incorrect melting of the built layers and the spherical due to gaseous argon in the raw powder [13]. Depending on the building direction of components the pores may affect the mechanical properties differently. Porosity between layers could decrease the yield strength and UTS of samples strained perpendicular to their layer orientation [15]. The effect of pores could be more limited in samples with layer orientation parallel to the tensile direction, since those samples will not include as many layers and thus possibly decrease the risk of pores being present [15]. According to the producers, delivered materials should have mechanical properties as shown in Table 2 and Table 3.

Table 2 - Key mechanical properties for EBM produced components.

	EBM as-built
Yield strength (MPa)	950
UTS (MPa)	1020
Elongation to fracture (%)	14
Hardness (HV)	327

Table 3 - Key mechanical properties for SLM produced components with varying building direction, X (horizontal) and Z (vertical).

	SLM as-built	SLM heat treated
Yield strength X (MPa)	1060 ± 50	1000 ± 20
Yield strength Z (MPa)	1070 ± 50	1000 ± 20
UTS X (MPa)	1230 ± 50	1050 ± 20
UTS Z (MPa)	1200 ± 50	1060 ± 20
Elongation to fracture X (%)	10 ± 2	14 ± 1
Elongation to fracture Z (%)	11 ± 3	15 ± 1
Hardness (HV)	320 ± 12	320 ± 12

2.3. Effect of surface roughness

Surface roughness will affect mechanical properties of components. Different manufacturing processes such as EBM and SLM generate different surface roughness depending on process parameters and powder sizes. The surface roughness of EBM produced components are usually worse than that of SLM. The SLM building process is generally one order of magnitude slower than the EBM building process resulting in higher productivity but worse surface quality for EBM components. However, there are several other parameters which affect the surface roughness such as, powder size, layer thickness and strength of the beam [12].

To maintain sufficient surface properties with high productivity, process parameters are usually different during melting of the outer contours in each layer than the remaining bulk build area. This method is good for surface tailorability since roughness properties can be controlled independently from the bulk process parameters. Usually a lower beam current and scan speed is used on the contours [16].

For powder bed fusion processes such as EBM and SLM there are no gaps between the built parts and the un-molten powder. Thus, these parts have similar surface roughness to sand cast metallic components and the diameter of the powder affects the degree of roughness [17]. Reasons for surface roughness in additive manufactured parts partly relates to un-molten powder or from powder which has been sintered onto the surface, see Figure 6 [16, 18]. There are several process parameters which affect the melting or sintering of powder. High beam current and slow scan speed will generate a larger melt pool which yields worse surface roughness [16].

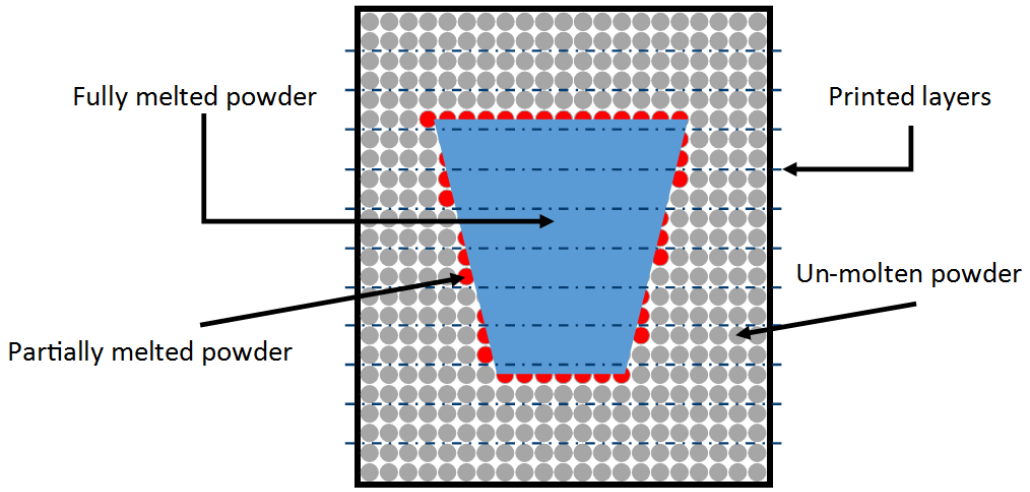

Figure 6 – Illustration of partly molten powder sintered to the surface of a fully dense component.

Roughness of EBM parts is related to preheating of the powder. Since the entire build chamber is preheated, the powder around the component is also preheated. Preheated powder requires less energy to sinter or melt. The powder which is in direct contact with the built component has easier to sinter to the surface, this results in a rougher surface than for SLM processes [16].

Surface roughness can determine how a component performs mechanically. Rougher surfaces give more sites for crack initiation because local stress concentrations are higher, as illustrated in Figure 7. Small internal cracks, surface defects or porosity can also be locations for crack initiation [19].

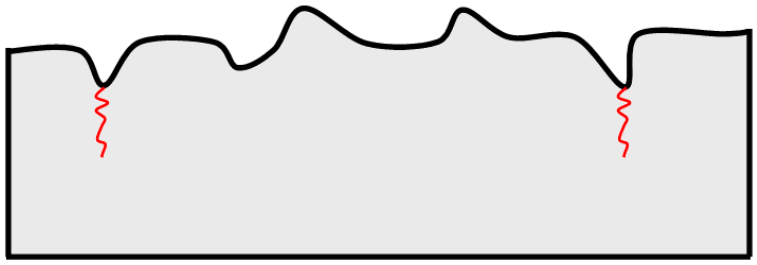

Figure 7 – Local roughness on sample acting as initiation for cracks.

2.4. Digital Image Correlation (DIC)

Utilizing DIC for detection of strains starts by taking a series of images of an altering surface. The first image is divided into a grid of facets (or subsets) and used as a reference. The facets can be overlapped with a specified step size in order to increase the spatial resolution, see Figure 8. The DIC software correlates the remaining images in the series to the reference and searches for the facets in each of these. Each facet should contain a unique pattern to be found in each subsequent image. As the sample is strained the displacement of each facet can be recorded, see dX and dY in Figure 10. The magnitudes of these displacements can be recalculated into strains and are often illustrated by different colors in the DIC software as can be seen in Figure 9. The images are analyzed in grey scale which means that the images needs to have high contrast and sufficient gray-scale difference so that a unique pattern in each facet can be obtained [20].

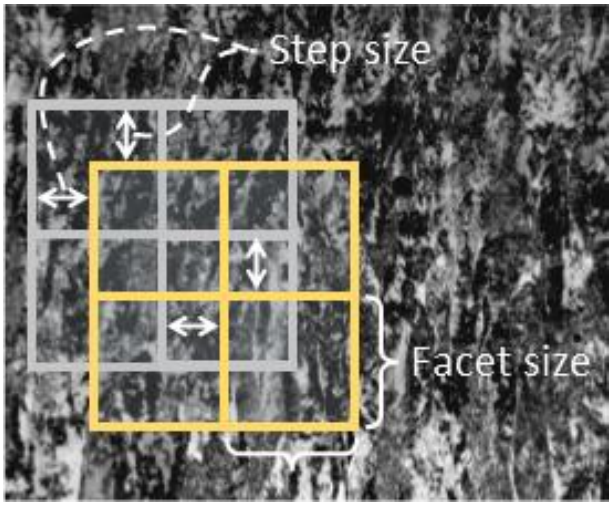

Figure 8 – Illustration of facet size and step size.

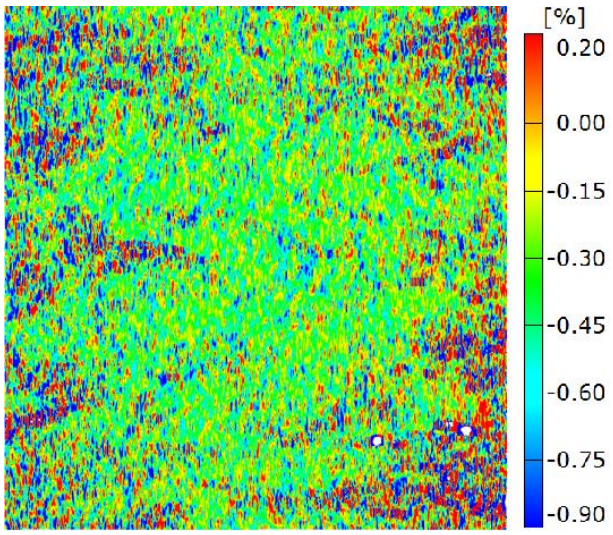

Figure 9 – Illustration of strain field from DIC analysis.

Facet and step size are critical analysis parameters for the DIC software which affects the strain resolution and the spatial resolution. The strain resolution is the minimum resolvable strain level defined as the noise level, strains lower than the noise cannot be perceived as true. A trade-off between chosen step size and facet size is needed to tailor the output data. An increased facet size will decrease the spatial resolution, compare Figure 10 with Figure 11 where Figure 10 has smaller facet size (X,Y < X2,Y2) and thus higher spatial resolution. However the facet size should be sufficiently large to allow for good correlation between the images. Larger facets have more unique information within them. A good correlation will minimize the noise of the strains and thus increase the strain resolution [21].

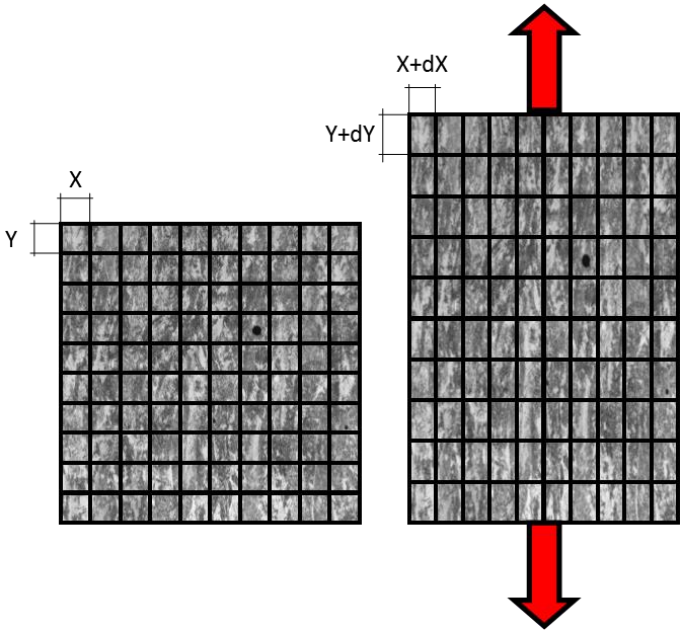

Figure 10 – Illustration of displacement in smaller facets.

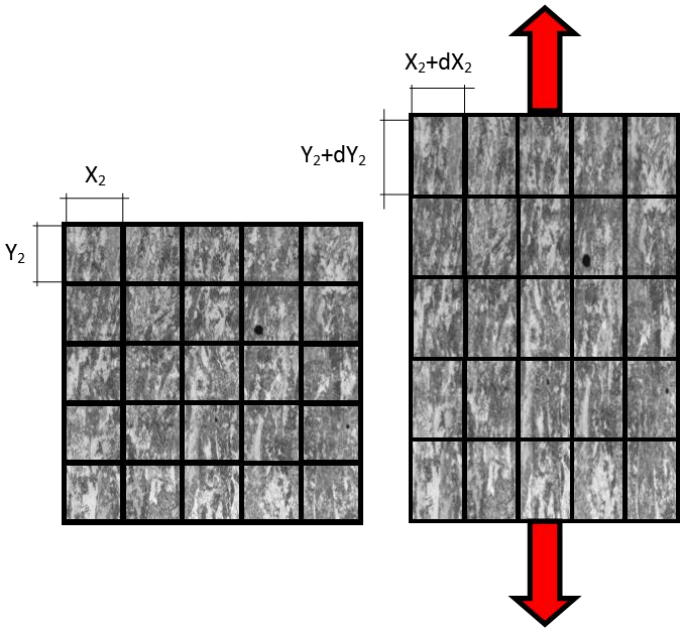

Figure 11 - Illustration of displacement in larger facets.

It has been shown that losses in spatial resolution are more severe when increasing the step size than by increasing the facet size. The optimal selection of parameters is to keep the facet size at a good level of correlation and lower the step size to reach the best spatial resolution possible [21].

When performing a static tensile or compression test DIC can be used to study the strains or displacements of the surface. These can be analyzed in both macro and micro scale using different lenses. To be able to use the DIC analysis on test bars in macro scale a random speckle pattern is applied. When using a microscope lens the natural microstructure can be used as pattern [22].

3. Method

This section includes the stages of how the project has been conducted, information concerning material and testing procedures are presented.

3.1. Material

Samples were provided from Arcam AB and Lasertech LSH AB manufactured from Ti-6Al-4V powder that has a composition according to ASTM F2924, see Table 1. The samples were produced from a CAD file provided by SP with slightly larger dimensions than the final design which can be seen in Figure 12. Samples delivered from Lasertech were manufactured using SLM with average powder diameter of approximately 50 µm and layer thickness of 60 µm. Arcam used EBM with powder diameter between 45-100 µm and layer thickness of 70 µm. The mechanical properties according to the companies can be seen in Table 2 and Table 3.

Both companies made two different layer orientations, one set was built parallel to the tensile direction (X) and another perpendicular to the tensile direction (Z), see Figure 13 and Figure 14.

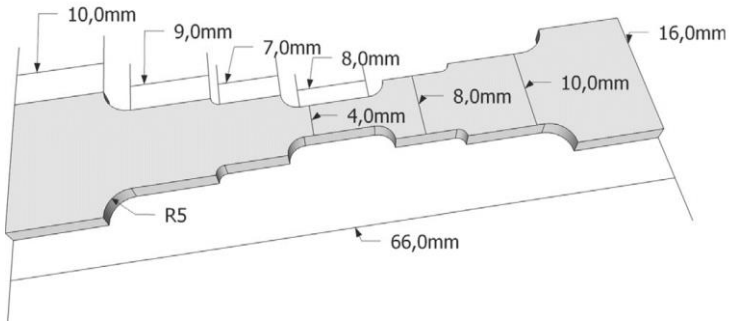

Figure 12 – Dimensions of the sample.

Half of the samples produced with SLM were heat treated for three hours at 600°C in an argon/vacuum environment for stress relief. An index of the samples with different manufacturing parameters can be seen in Table 4.

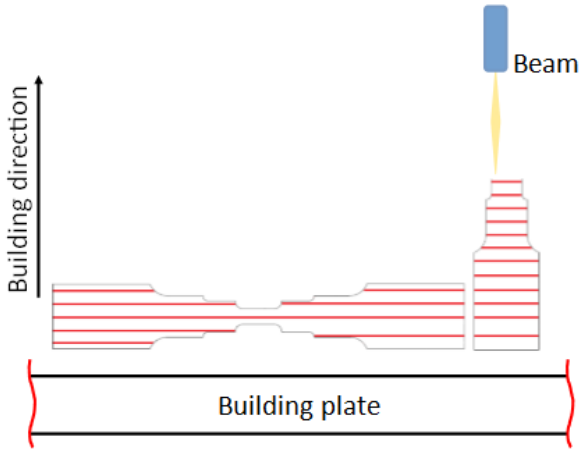

Figure 13 - Shows the two different sets of samples being produced, the left sample has a layer orientation parallel to the tensile direction (X) whilst the right sample has a layer orientation perpendicular to the tensile direction (Z).

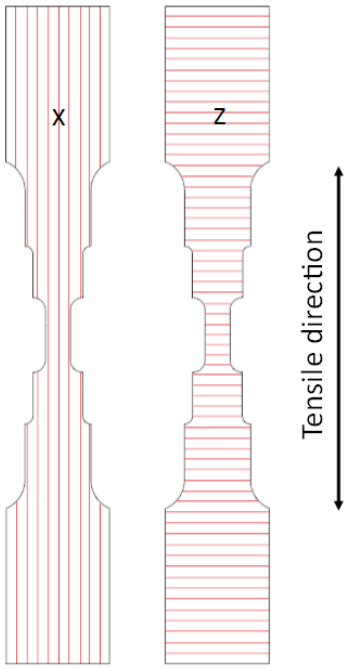

Figure 14 – Two samples with different layer orientation. The left sample have layer orientation parallel to the tensile direction (X) whilst the right sample have perpendicular to the tensile direction (Z).

Table 4 – Index of samples with different manufacturing parameters, # is the sample number.

Index	EBM	SLM	Orientation	Treatment
EBM-X-AB-#	X		Parallel	As-built
EBM-Z-AB-#	X		Perpendicular	As-built
SLM-X-AB-#		X	Parallel	As-built
SLM-Z-AB-#		X	Perpendicular	As-built
SLM-X-HT-#		X	Parallel	Heat treated
SLM-Z-HT-#		X	Perpendicular	Heat treated

3.2. Sample preparation

Samples from each set in Table 4 were milled in SP's workshop to the dimensions given in Figure 12. Struers ABRAMIN machine was used for grinding and polishing one side of each sample. The grinding process was split up into five steps each with a rotating speed of 300 rpm utilizing SiC papers with decreasing grit size and water as coolant/lubricant. In between each step the samples were submerged into an ultrasonic bath for approximately 120 seconds to clean them from particulates before moving to a finer grit paper. The stepping sequence set out with grit 500 for 150 seconds followed by grit 1000 for 120 seconds and grit 4000 for 70 seconds. A force of 30 N/sample was applied during each grinding step. During the last 30 seconds with grit 4000 the force was lowered to 10 N/sample.

The polishing process was split up into two steps. The first ran for 120 seconds with an MD-DUR plate and rotation speed of 150 rpm. During this step the MD-DUR plate was sprayed with 3 μm OP-s solution, a red water based DP-lubricant was continuously sprayed onto the plate during polishing. A MD-Chem plate was used for the second step which ran for 80 seconds, the plate was continuously sprayed with a mixture of 90 wt% 0.04 μm OP-s solution and 10 wt% H_2O_2 (30% concentration). After polishing, the EBM samples were etched for approximately 60 seconds and the SLM samples for approximately 180 seconds. The etchant was mixed according to Kroll's Reagent (Hydrofluoric acid (40%) 2 ml, Nitric acid 2 ml, distilled water 100 ml).

The side for macro analysis was kept as-milled and just before the tensile test it was painted with a white color followed by speckling of a unique black pattern. The painted side is shown in Figure 15.

Figure 15 – Speckled pattern on sample for macro analysis.

In addition to the main sample preparation explained above, prior to milling, test-pieces from each set of materials were cut using Struers Labotom-3 cutting machine. These were embedded in epoxy. After this the samples were ground and polished in the same manner as the main samples for subsequent analysis and hardness testing.

3.3. Hardness test

The Vickers hardness test (Zwick/Roell ZHM) was performed on the polished surfaces with 2000 g load.

The tests were performed on all six of the embedded samples. In total 40 indention was made on each sample and an average with standard deviation was calculated. The indention pattern was 10x4 indentations with a distance of 500 μm x 500 μm between the indentions. Measurements of the indentions were performed automatically by the machine.

3.4. Tensile test

The tensile test was performed at SP utilizing an in-house built tensile test machine with a maximum load capacity of 10 kN. The two cross-heads were moved simultaneously in opposite directions to make sure that the center of the sample was fixed during the whole test. The tests were performed in room temperature with constant cross-head speed of 0.00022 s^{-1} which is according to SS-EN ISO 6892-1:2009. The samples were mounted in the machine with a fixture on the cross-heads which does not require any clamping force as depicted, Figure 16.

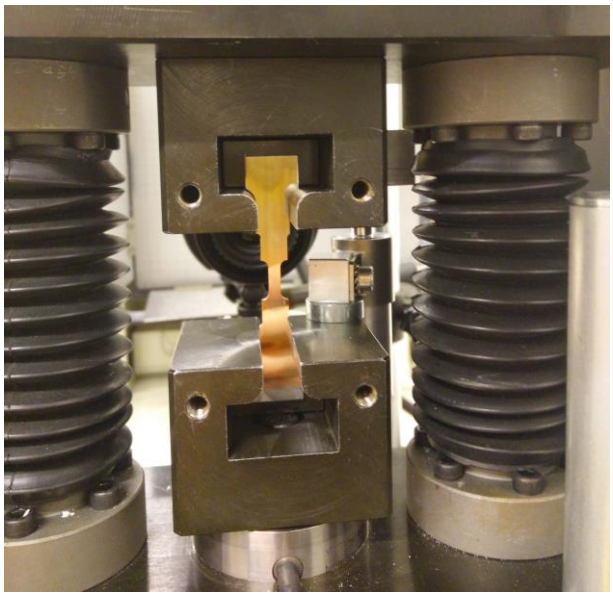

Figure 16 – Tensile test machine showing both cross-head fixtures and a mounted sample. This setup will result in that all load is applied on the radii of the samples and no clamping force is required.

Load data was acquired from a load cell (max 10 kN) to an in-house program at 10 Hz. This data was also continuously sent to the DIC system.

3.5. Digital Image Correlation

Full-field Strain measurements were carried out using GOM ARAMIS DIC system. Two 2D strain fields were obtained during the tensile test, one from each side of the sample. Two 4 Megapixel CCD-4000G cameras were used for the image acquisition, the cameras were aimed at separate sides of the sample according to Figure 17. The camera using a macro-lens was arranged so that the side of the sample with a speckled pattern was visible, see Figure 15. The other camera was equipped with a 5x objective lens arranged towards the center of the etched side. The visible area on the sample surface corresponds to approximately 3x3 mm^2 for the microscopy side and the entire sample area for the macroscopy. Since 2D measurement was used, no calibration of the cameras was needed.

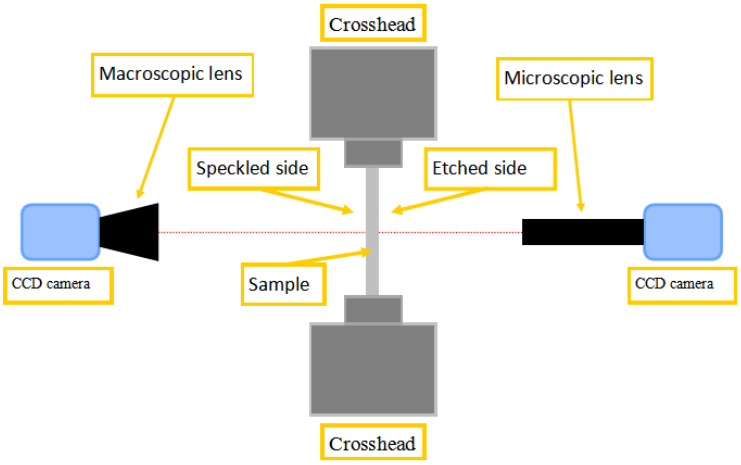

Figure 17 – Illustration of camera setup for data collection.

Prior to testing the shutter time and camera lights were adjusted to remove any over exposure. Two images were taken manually for calculation of standard deviation which will be the noise of the analysis (which was lower than 0.1 % for all tests). The images were masked to only include areas of interest. A starting point with high contrast and good focus was selected on the first image in order to start the correlation. During the tensile test the DIC system acquired one image every four seconds from each camera.

As mentioned in section 2.4 the chosen facet size and step size is critical in order for detection of strain gradients with sufficient accuracy. Through both manufacturing methods analyzed in this study the reported layer thickness is approximately 60 μm and some fusion between them is to be expected. In order to differentiate between strains in separate layers a step size needs to be selected so that enough data points (facets) are present within the 60 μm range. The facet size for the macroscopic strain fields was set to 20x20 pixels (approximately 360x360 μm) with a step size of five pixels (approximately 90 μm) and for the microscopic field 30x30 pixels (approximately 45x45 μm) with step size of ten pixels (approximately 15 μm).

From the different lenses, calculations of how a physical distance on the surface correlated to one pixel in the images were made. With the macroscopic camera one pixel correlated to approximately 18 μm, this removes the possibility of detecting any strains within the 60 μm span. However, with the microscopic lens it was found that one pixel correlated to approximately 1.5 μm. By selecting a facet size of 30x30 pixels for the microscopic analysis it ensured that each image would include enough information for an accurate strain presentation. By tailoring the step size so that at least ten strain values within the 60 μm range was present a step size of four pixels was selected for a second microscopic analysis. Calculation with this lower step size was applied on only six microscopic tests due to limitations in data storage and computation time.

3.6. Light optical microscope

Light optical microscope was used in order to analyze the microstructure of all the samples. This was performed on the etched surface at three different magnifications (50x, 200x and 1000x). Several images were collected from all the different magnifications. All the samples were oriented so that the building direction was shown upwards in the images.

3.7. Measuring uncertainty

Data gathered from the machines have uncertainties which affect the accuracy of the results. The load cell used for collection of force during the tensile test has an uncertainty $< \pm 0.25$ %. The sample dimensions are measured using a micrometer with an uncertainty $< \pm 0.1$ %. Strains are obtained from the GOM ARAMIS DIC software using the images taken during the tensile test, these strains have resolution of $< \pm 0.1$ %. It should be noted that pseudo strains might be present since the surfaces distance to the cameras might vary during the test. Especially above yield were the surface is plastically deformed in all directions. Also to be noted is that dust can be present on the image sensor resulting in loss of correlation in these specific areas. During the tests this can be seen in the microscopic strain fields, the data around these areas should not be used as a material parameters. Accuracy of hardness values are given from the type of indentions. HV 1-100kg have an uncertainty $< \pm 2.1$ %, according to SPs internal data. From final machining

of the samples, the radii in contact with the fixture of the tensile test machine could have alternating dimensions. This could result in a bending moment seen in some samples during the tensile tests.

Calculating the combined uncertainty up to yield stress (U_{stress}) requires consideration of the load cell as well as the micrometers accuracy. The stress uncertainty up to yield is calculated according to equation below, according to SPs internal data. Where uncertainty of the area due to calculation using two separately measured values is < ±0.2%.

$$U_{stress} = 2 * \sqrt{0.25^2 + 0.2^2} < 1\ \%$$

The measurement uncertainty for the tests is shown in Table 5.

Table 5 – Measurement uncertainty for collected data.

Measurement	Measuring uncertainty
Stress	± 1 %
Strain resolution	± 0.1 %
Hardness	± 2.1 %

4. Results and Discussion

This section contains results and discussion from the tests performed.

4.1. Optical microscope

For all samples it can be seen that the grains have grown in an epitaxial manner in the same direction as the building direction shown in Figure 18. An explanation for this is the re-melting of layers when a new layer is applied as explained in chapter 2 [11, 23].

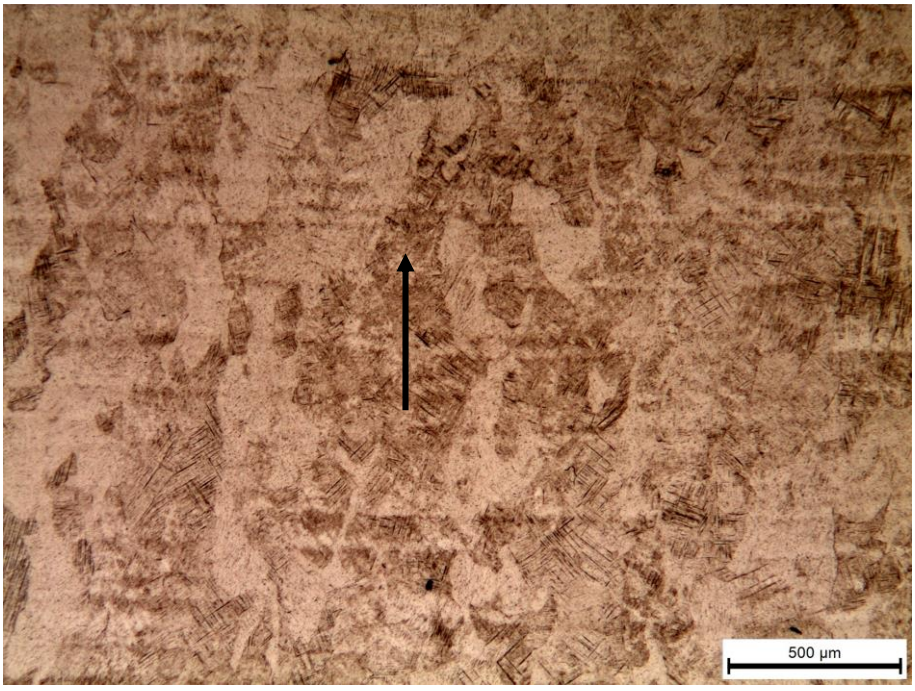

Figure 18 – Microstructure of SLM-Z-HT at the magnification of 50x, building and grain direction is upwards, see the black arrow.

The main difference between X-samples and Z-samples is that the Z-samples show more distinct indication of layers in form of lines perpendicular to the building direction. This was true for both EBM and SLM samples. These layer indications might be a combination of the etching and the orientation of which the beam melts the powder. According to the producers the melt path of the beam is shifted 66° in between each layer during building. This change of melting orientation could cause the etchant to display the layers in different contrasts. To the authors knowledge this has not been reported before. It should also be noted that the SLM samples had stronger indications of layers than the EBM samples. This can be seen by comparing Figure 19 with Figure 20. It has also been observed that the as-built SLM samples have stronger indications of layers than the heat treated SLM samples, compare Figure 18 with Figure 20. Through these comparisons the magnitude of layer indication could be connected to the time temperature history of the samples. As-built SLM samples have the least time at elevated temperature followed by heat treated SLM samples and then the EBM samples. A higher layer indication can thus be connected to lower time at elevated temperature.

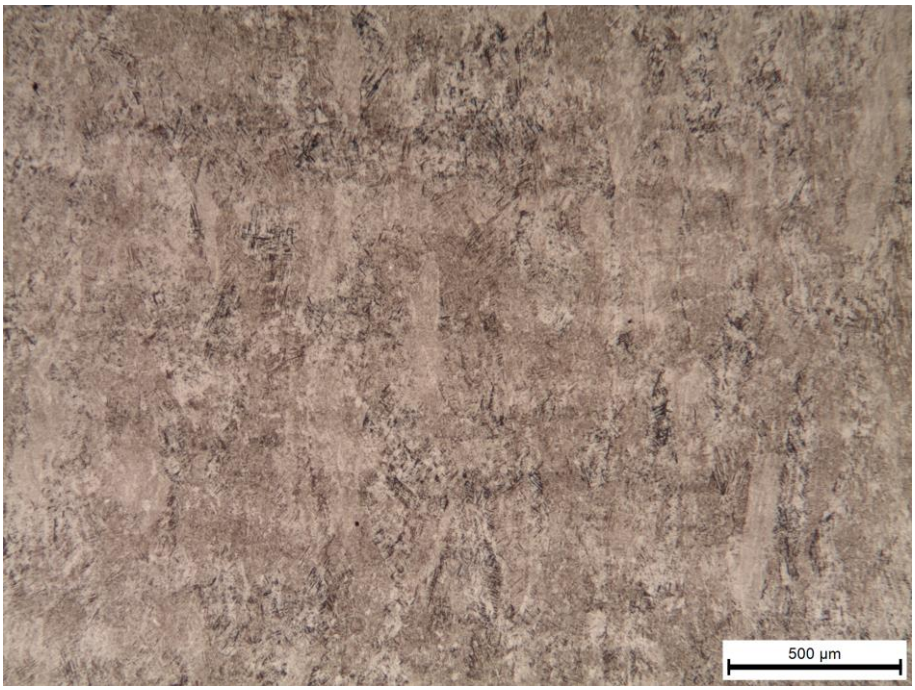

Figure 19 - Microstructure of EBM-Z-AB at the magnification of 50x.

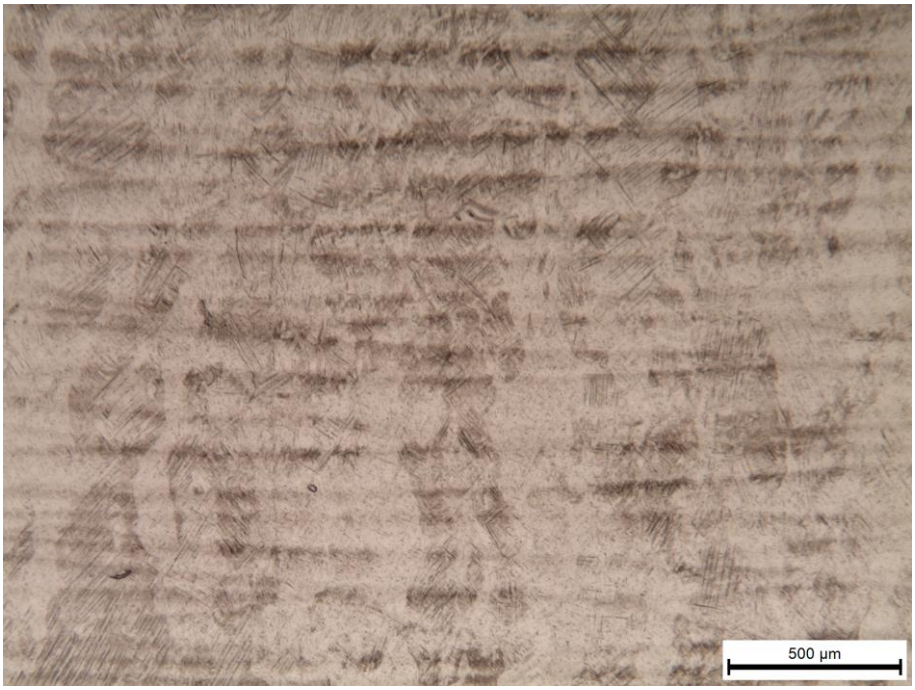

Figure 20 - Microstructure of SLM-Z-AB at the magnification of 50x.

The as-built SLM samples show a fine α' microstructure as can be seen in Figure 21 where the columnar β-grains will be filled with acicular α' laths shown at lower magnification Figure 24 [24]. The as-built EBM samples show α+β microstructure, see Figure 22. These features are well documented and explained by rapid cooling of SLM samples and the pre-heating of the EBM samples [10, 11, 13].

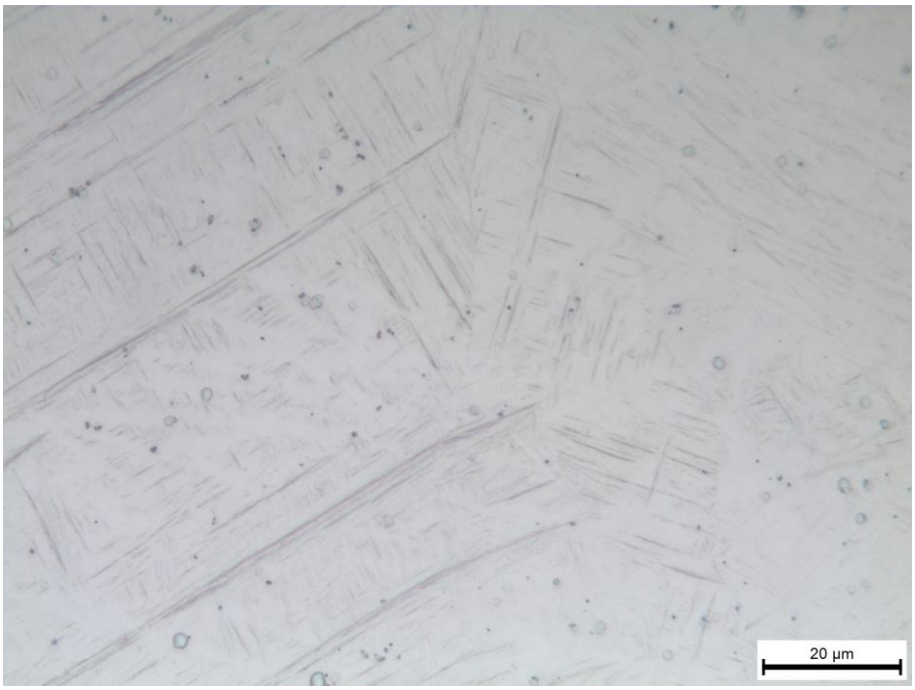

Figure 21 – Microstructure of SLM-X-AB at the magnification of 1000x.

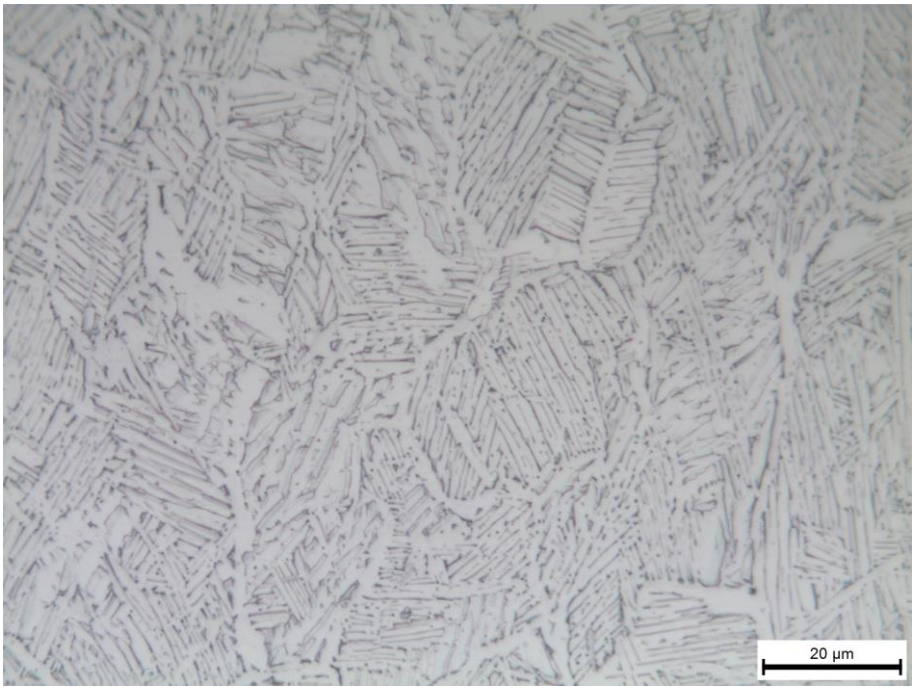

Figure 22 – Microstructure of EBM-X-AB at the magnification of 1000x.

Heat treated SLM samples have a microstructure in between both EBM and as-built SLM samples. The heat treatment will not change the prior β-grains of the SLM samples since the temperature is much lower than the β-transus temperature. However, the phase composition will be changed since the heat treatment will transform the α' into a mixture of α and β phases. In Figure 23 the bright phase is β and the dark laths are α. The α (prior α') laths in SLM samples span over the width of a prior β-grain as shown in Figure 23 and Figure 24, comparing these two figures indicates that the heat treatment will thicken the laths [15].

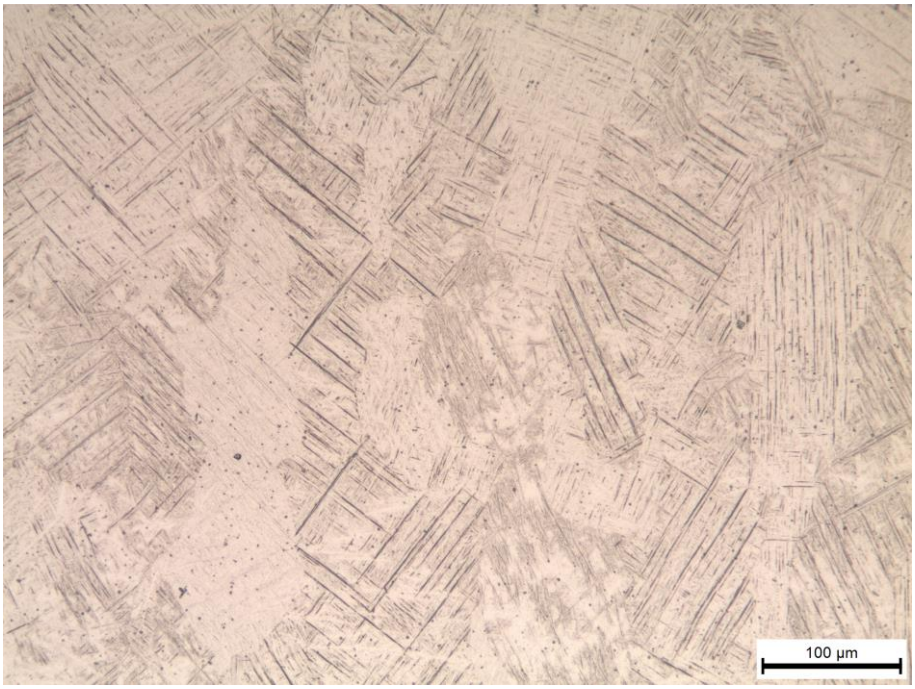

Figure 23 – Microstructure of SLM-X-HT at the magnification of 200x.

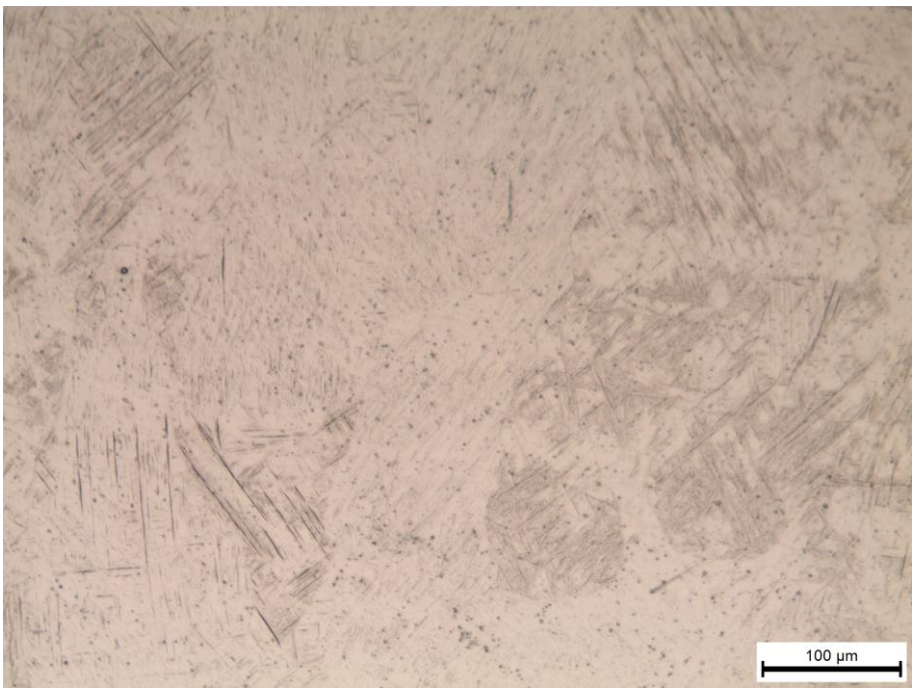

Figure 24 – Microstructure of SLM-X-AB at the magnification of 200x.

In one of the EBM samples lack of fusion has been seen and is shown in Figure 25. Pores have been detected in both SLM and EBM samples, shown in Figure 26. Usually the origin of gas pores is connected to the gas atomization process of the powder, where powder particles might contain argon [22]. In general, both processes did not show a lot of pores nor lack of fusion.

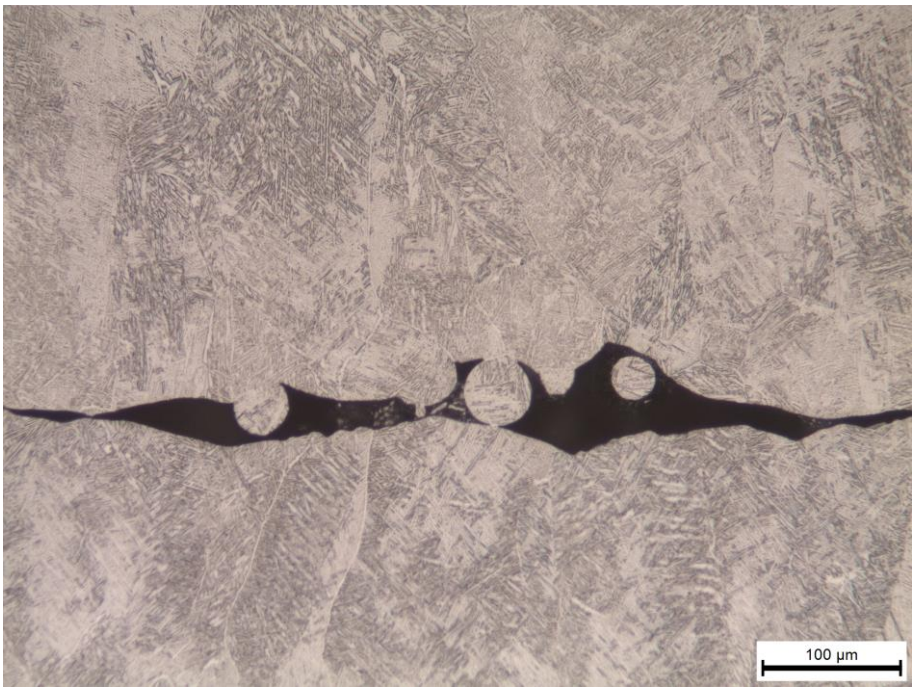

Figure 25 – Microstructure of EMB-X-AB at a magnification of 200x.

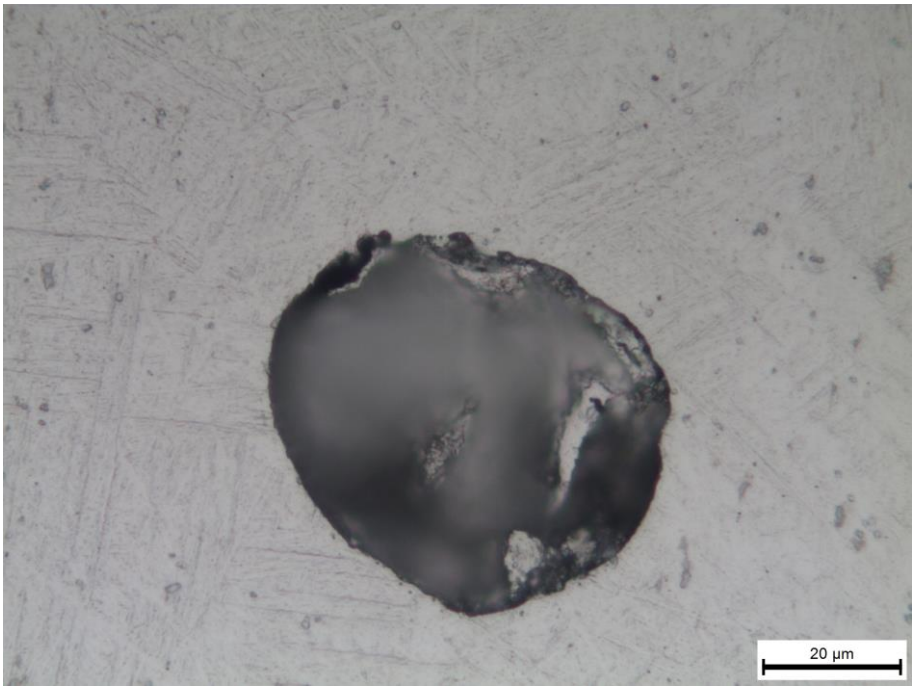

Figure 26 – Microstructure of SLM-Z-HT at a magnification of 1000x.

Darker and brighter fields widely seen in SLM built samples were analyzed in a software called ImageJ. Through a function called plot profile the greyscale variation following a set line crossing the layers was plotted according to Figure 27. This plot strengthens the theory that the visible fields in fact are indications of layers since the distance between a high and low grey value is between 50-100 μm. The reported un-melted powder layer should be 60 μm in the SLM built samples.

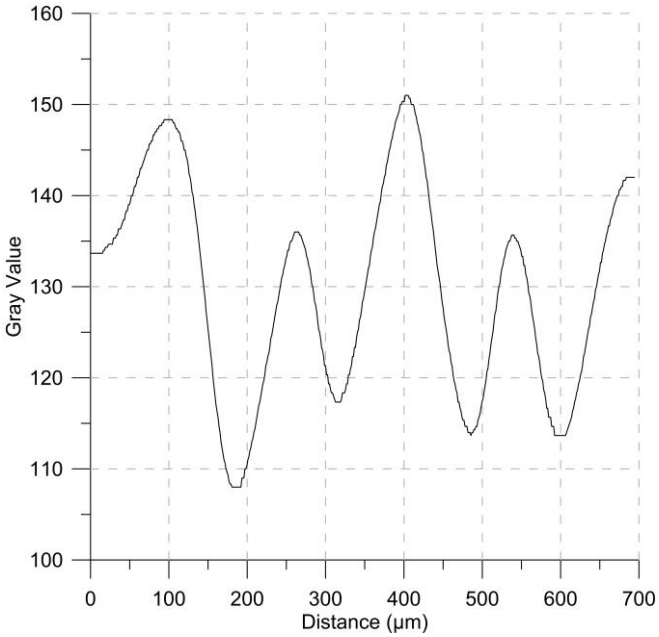

Figure 27 – Grey scale difference as a function of distance across a line perpendicular to the built layers in sample SLM-Z-AB.

4.2. DIC-analysis

This section includes result and discussion concerning strain fields collected by the microscopic DIC-analysis. The presented fields are visualizations of strains in the tensile direction, indicated as "epsilon Y" in the DIC software images. The focus will be on determining how the fields differ depending on manufacturing process and building direction and to connect local strains to the microstructure visible in the raw images. The color scale for the strain field images have been fixed so that results from different samples are comparable at their individual stress values.

Indications of different strains in different layers should be shown as continuous elongated strain concentrations parallel to the layers [22]. This behavior has not been seen in any samples regardless of building direction and manufacturing process. Which indicates that the material with respect to individual layers is homogeneous.

In all of the strain fields the alternating positive and negative strains visible close to each other could be the result of pseudo strains, since in a 2D DIC analysis a movement away from the camera is regarded as a positive strain and movement towards the camera regarded as a negative strain. The local out-of-plane movement might be due to local yielding. After fracture it can be seen by the naked eye that the surface of the polished sample has been deformed and become rougher. This supports the statement of localized pseudo strains.

4.2.1. EBM strain fields at yield stress

Results from the DIC analysis in terms of strain fields at yield stress indicate that the X-built EBM samples contain localized strain concentrations elongated perpendicular to the tensile direction. This localization can be viewed in Figure 28 and potentially be connected to the texture of the prior β-grains. To the center-left of the strain field image in Figure 28 the local strains seem to intertwine with a grain seen at same location of the non-analyzed image highlighted with red. The Z-built EBM sample shown in Figure 29 seem to have localized strain fields elongated in the tensile direction. This can be seen as elongated strain concentrations in center of the strain field image in Figure 29 marked with blue dashed lines. The grain texture of EBM-Z samples are parallel to the tensile direction. Comparing X- and Z-built samples indicates that individually built layers might not affect strains as much as the alignment and texture of the microstructure.

If there are large areas of local strain concentrations present in a strain field, the variance, and thus the standard deviation, of the strain distribution will be larger. The magnitude of the standard deviation can thus give an indication of the homogeneity of the strain field. By comparing the standard deviation of the strain fields from each build direction both appear rather inhomogeneous, see Table 6. The tabulated values does not say much until the actual images are looked at. Generally it can be seen that the X-built samples experience strain in the Y direction though local deformation of individual softer grains perpendicular to the tensile direction, which can be seen by following a vertically drawn line in the strain fields. This behavior is also seen in the Z-built samples, however, since the grains are oriented parallel to the tensile direction the local strain concentrations seems to be distributed over several grains perpendicular to the tensile direction.

Table 6 – Global strain and distribution of EBM samples.

	Global strain at yield	Standard deviation
EBM-X-AB	1 %	±0.57 %
EBM-Z-AB	1 %	±0.54 %

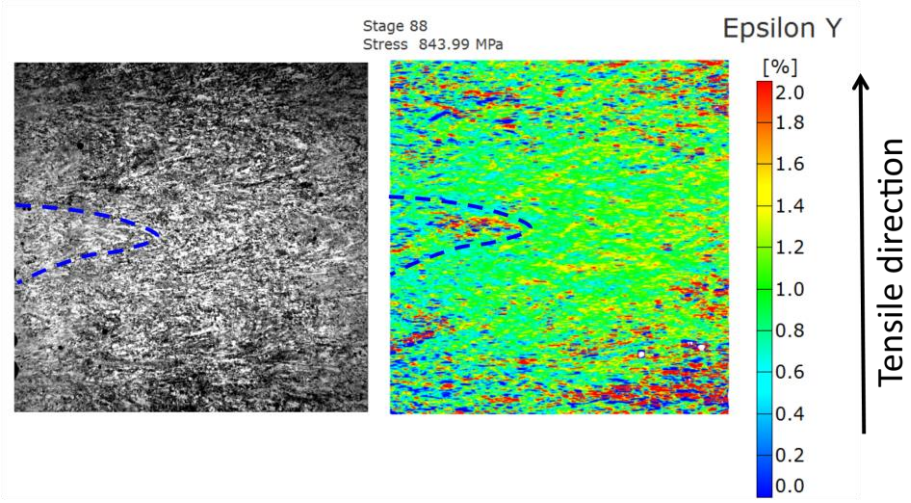

Figure 28 – Strain field of EBM-X-AB at yield stress.

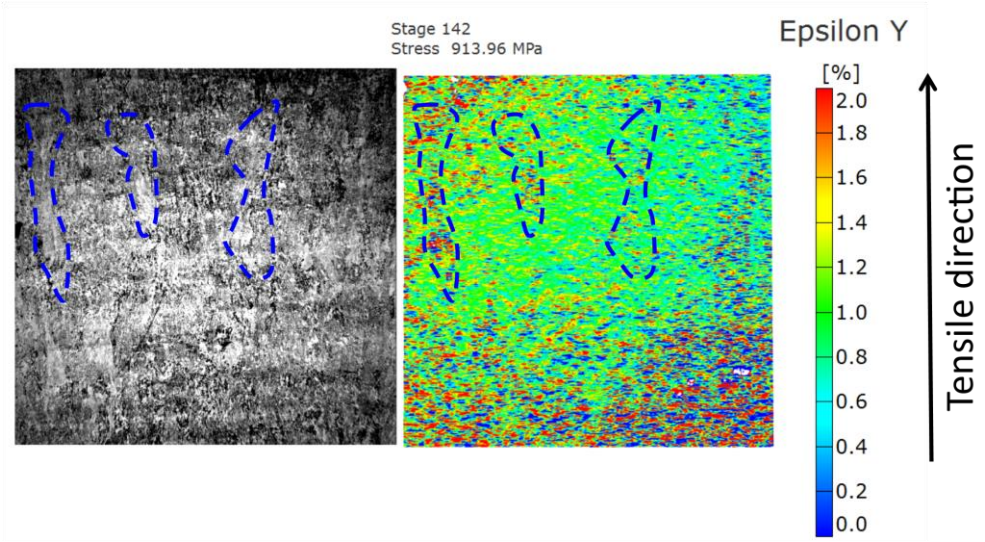

Figure 29 – Strain field of EBM-Z-AB at yield stress.

4.2.2. SLM strain fields at yield stress

By visually comparing the strain fields of the SLM samples generally it can be noted that the strain fields are more homogeneous in the Z-built samples shown in Figure 31 and Figure 32 in comparison to the strain fields shown in Figure 33 and Figure 34. However, this pattern cannot be significantly supported by comparing the global strains and the standard deviations in Table 7.

Table 7 - Global strain and distribution of SLM samples.

	Global strain at yield	Standard deviation
SLM-Z-AB	1.2 %	±1 %
SLM-Z-HT	1.1 %	± 0.5 %
SLM-X-AB	1.2 %	± 1.2 %
SLM-X-HT	1.2 %	± 1.1 %

Reason for this could possibly be connected to the preferable crack path of vertically or horizontally built samples discussed in [15]. It might also be connected to load distribution on the prior β-grains. A cross-section perpendicular to the tensile direction would reveal less grains in X-built samples than in Z-built samples, thus the presence of a weaker grain might have a larger impact on the samples built in X-direction.

In the strain fields of the Z-built samples to the right in Figure 31 and Figure 32 there seem to be a connection between local strains and individual grains, it can also be noted that in some cases the brighter fields of the microstructure contains strains of higher magnitude, see Figure 30.

Comparing the strains fields of the X-built samples both of them seem to have local strains elongated parallel to their prior beta grains. The thickness of these local strains does not seem to cover an entire thickness of a grain. However, they do seem to be located at positions close to the boundaries between grains. This finding is in good correlation with previous reports indicating that the preferable crack path for both heat treated and as-built SLM is intergranular [15].

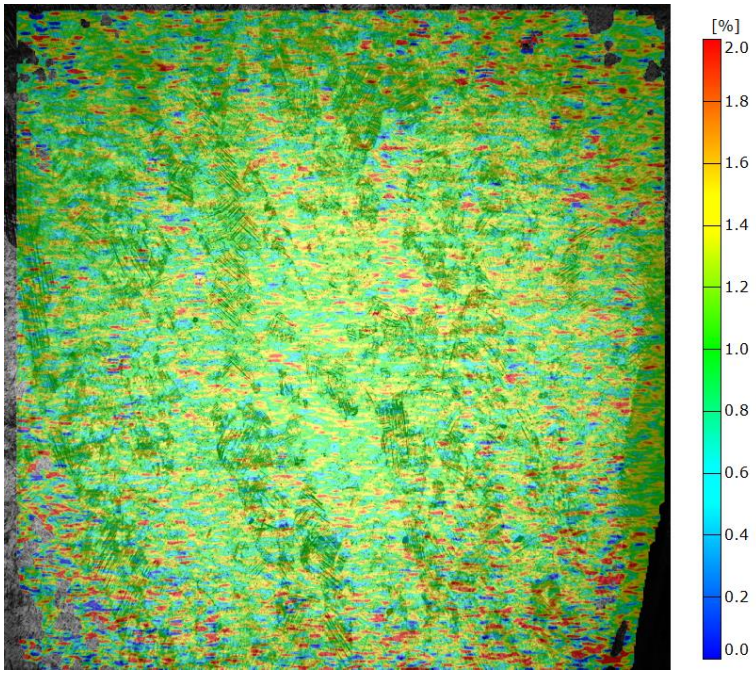

Figure 30 – Overlay image of SLM-Z-HT at yield.

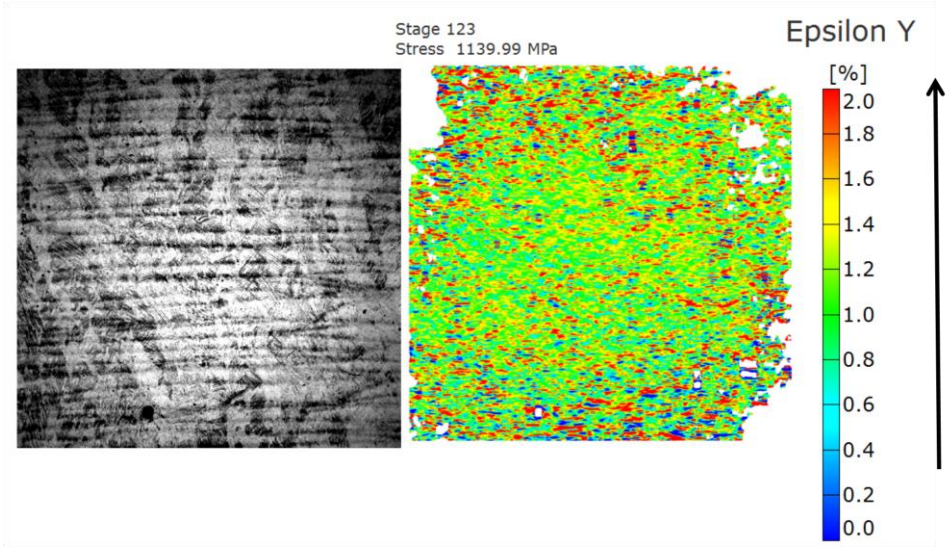

Figure 31 – Strain field of SLM-Z-AB at yield.

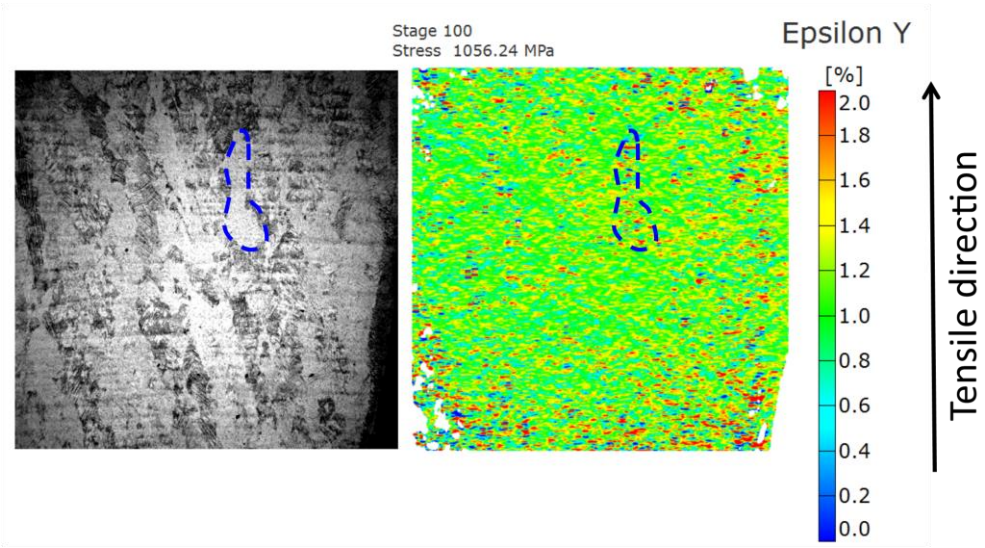

Figure 32 – Strain field of SLM-Z-HT at yield.

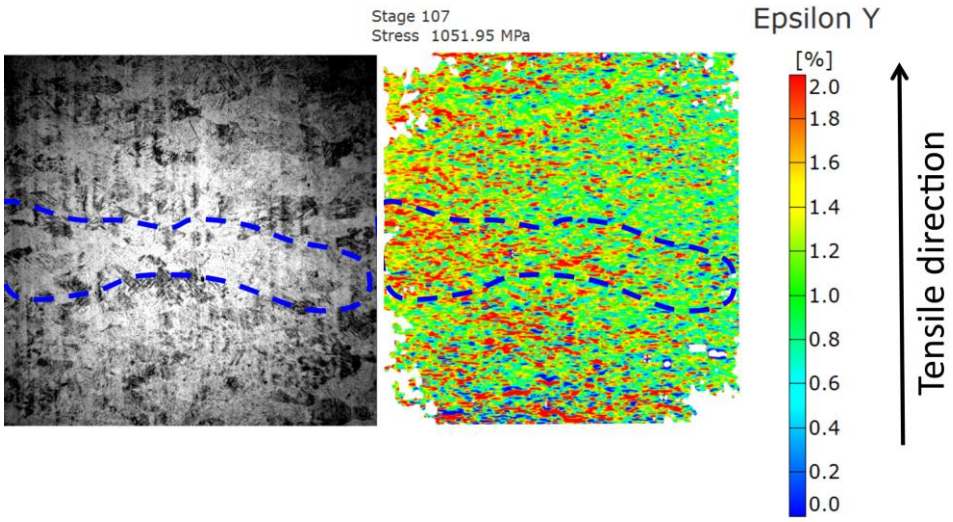

Figure 33 – Strain field of SLM-X-AB at yield.

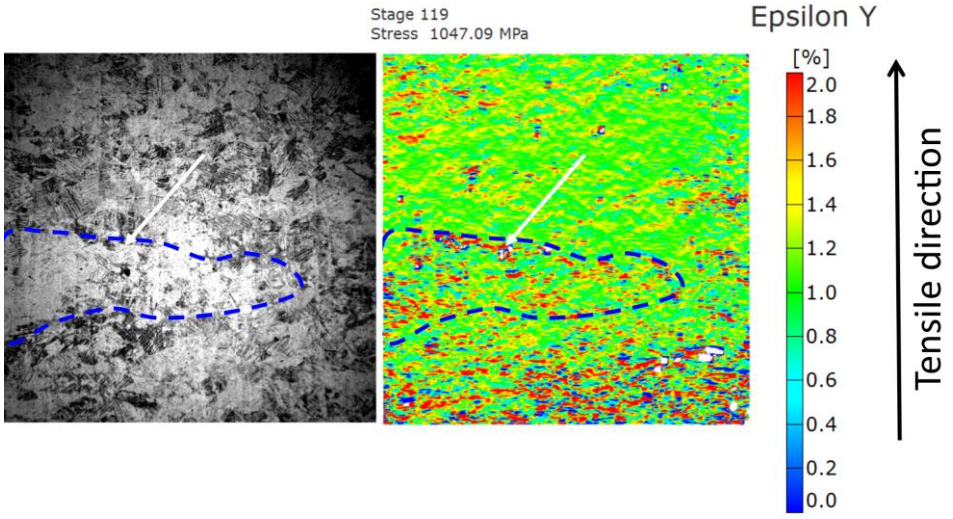

Figure 34 – Strain field of SLM-X-HT at yield

4.3. Mechanical Performance

Three samples from each batch were tensile tested. Young's modulus, yield strength ($R_{p0.2}$), ultimate tensile strength (UTS) and elongation at break were obtained and are tabulated in Appendix 1. A mean value and a standard deviation will be reported and evaluated. All tensile test curves are plotted and shown in Appendix 2. In addition results from the hardness tests will be evaluated and tabulated in Appendix 1.

Strain fields collected from the macroscopic DIC-analysis is used to export global strain information during the tensile test. Initially the data from the linear displacement sensor was used. However, it was shown that the extent of displacements in the actual tensile rig was too severe to fully trust its outcomes.

Generally it can be seen that samples built in the Z-direction have higher yield strength and UTS compared to the X-direction, see Figure 35 and Figure 36. It shall be noted that there is no significant difference in yield strength and UTS between SLM-X-HT and the SLM-Z-HT samples. However, the mean yield and tensile strength is higher for the samples built in Z-direction.

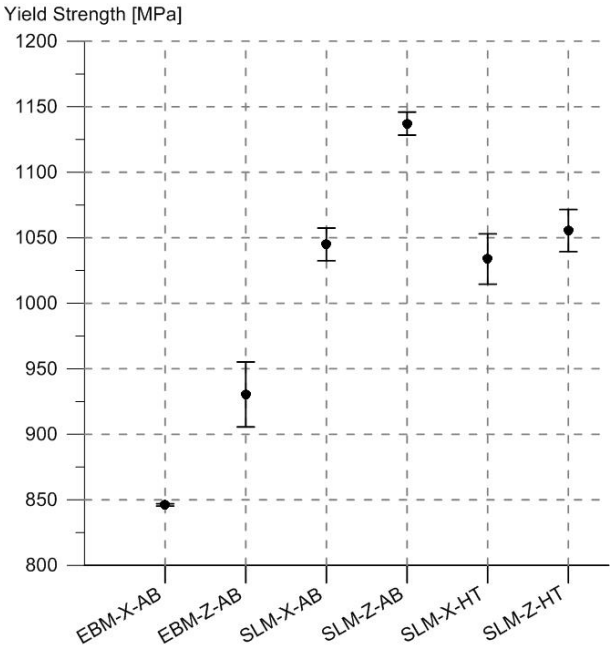

Figure 35 – Standard deviation plot of yield strength, the results are based on three tests within each batch.

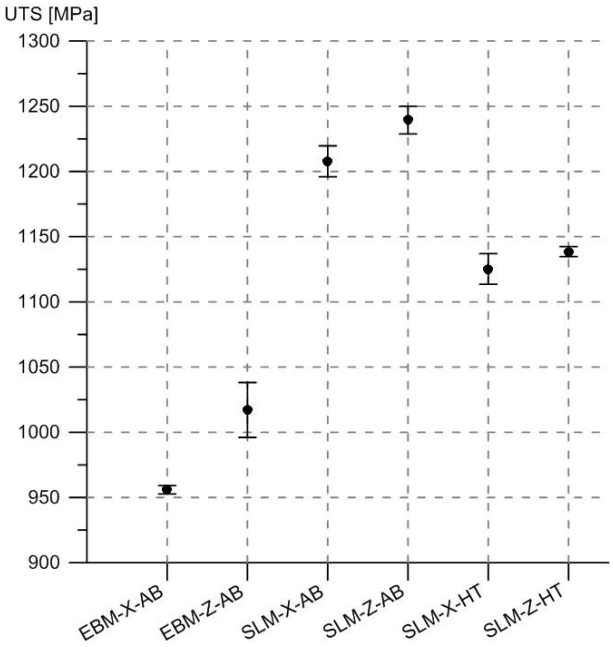

Figure 36 – Standard deviation plot of UTS, the results are based on three tests within each batch.

An explanation as to why Z-direction samples will have higher yield strength and UTS could be connected to the microstructure and especially the growing direction of the prior β-grains. These grains grow over several layers in the building direction, resulting in that all Z-direction samples will have prior β-grains along the tensile direction while all the X-direction samples will have the prior β-grains perpendicular to the tensile direction as shown in Figure 37.

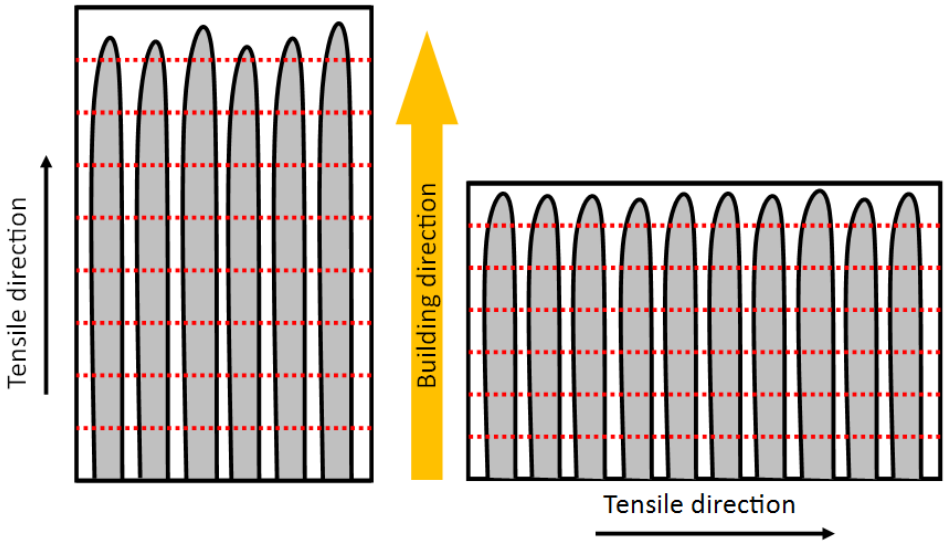

Figure 37 – Alignment of prior β-grains in reference to tensile direction, the left figure is Z-built and the right figure is X-built.

Comparing as-built SLM and heat treated SLM it can be seen that the UTS is lower for the heat treated samples, see Figure 36. This could be explained by the α' to α transformation and that the lath size increases during heat treatment, both of which results in lower UTS [15].

The increase of yield strength and UTS in the Z-built samples has previously been explained by an anisotropic behavior of the prior β-grains giving the Z-directional samples higher ability of crack deflection [15]. It has also been shown that the prior β-grain boundaries will be the preferable approach for crack propagation [25].

All SLM samples have higher yield strength and UTS than the EBM samples. This could be connected to the microstructure since α' will increase these two properties [13]. This is further confirmed by the hardness test, shown in Figure 38 . All SLM samples have similar hardness values but the EBM samples are deviating with lower hardness values. The hardness test only measures the surface hardness of a samples and not the whole cross-section. This in combination with that only one sample from each batch was tested could explain why the heat treated SLM samples, compared to the as-built SLM samples, do not have a lower hardness.

According to M. Simonelli et al. [15] the Young's modulus do not change with the building direction or the orientation of the prior β-grains. The test data from all samples shows that the Young's modulus ranges from 105 GPa to 124 GPa as shown in Figure 39. During the tensile test some of the samples were not evenly aligned due to insufficient milling of the radii connecting the sample to the crossheads. This introduced a bending moment on some samples and could be a reason for the large spread in Young's modulus.

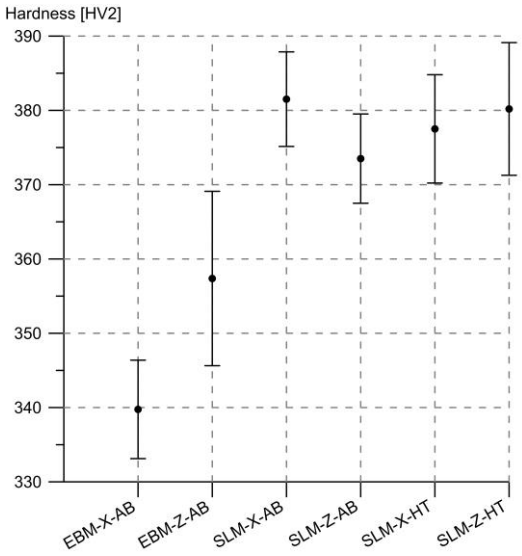

Figure 38 – Standard deviation plot of hardness, the results are based on 40 indentions on one sample in each batch.

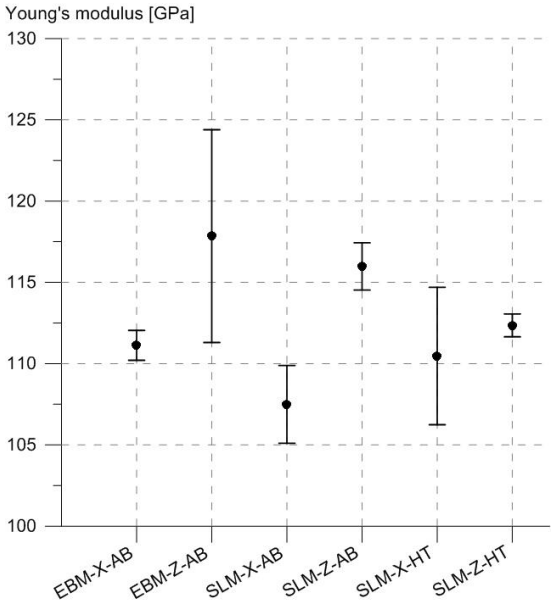

Figure 39 – Standard deviation plot of Young's modulus, the results are based on three tests within each batch.

By analyzing the ductility (elongation at break) no clear connection can be seen between the samples shown in Figure 40. This could indicate that the ductility is more related to defects rather than to the building direction or manufacturing process, as presence of defects would result in a non-homogeneous behavior [15, 22]. It is well known that the ductility will be controlled by defects such as pores and lack of fusion in layer-by-layer manufacturing methods [13, 22]. However, the optical investigation did not show large amount of defects. Even though there are no visible defect on most samples, it only takes one critical defect to drastically lower the ductility. This could explain why the deviation in ductility is high between samples.

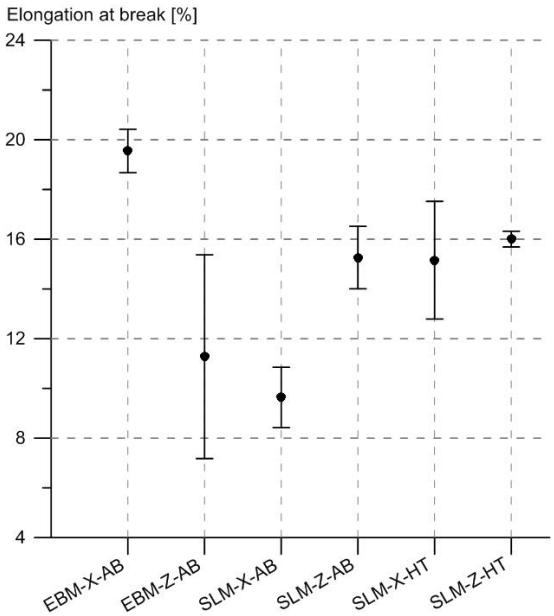

Figure 40 – Standard deviation plot of elongation at break, the results are based on three tests within each batch.

One of the large drawback in ductility for as-built SLM samples is the formation of α'-phase and presence of internal stresses, both of which will decrease the ductility of samples. A higher volume fraction of β-phase will increase the ductility by allowing slip transfer in the interface between two phases. The internal stresses will lower the ductility regardless of the building orientation. By heat treatment of the α' structure it transforms into a α+β-phase thus increasing the ductility of the SLM parts [13, 15]. This behavior has not been observed for Z-built SLM samples and a possible reason could be the presence of defects.

5. Conclusions

Both EBM and SLM manufactured samples have prior β-grains grown over several layers in the building direction. It has been concluded that additive manufactured materials will have anisotropic mechanical properties due to the alignment of these prior β-grains. By using DIC it have been shown that grains are regions for strain concentrations and that built layers might not be the cause for any anisotropic behavior. It is reasonable to assume that these regions of higher strains can act as initiation points for critical failure. These findings should be further studied in order to conclude if any precautions are needed regarding the building direction of components.

From this thesis it can be concluded that different mechanical properties are achieved from the different manufacturing processes. Samples manufactured using the SLM process has higher yield strength, UTS and hardness. This is linked to the microstructure of the materials and especially the α'-phase. By heat treatment of the SLM samples it has been seen that both the yield strength and the UTS decrease but the hardness remains the same. The differences in mechanical properties between the two processes are relatively small. Most of the mechanical data is in good agreement with previous reports, the focus in this report was to compare the mechanical properties together with the DIC analysis. Relatively small amounts of defects have been observed which indicates that both processes are well controlled and that both can produce high quality products. A conclusion cannot be drawn of whether SLM or EBM is the best manufacturing method since there always is a balance between profits and desired mechanical properties in products.

The research questions are answered as follows:

1) **Is there any obvious difference in mechanical performance depending on the building process?**
   Yes, it has been concluded that the two different manufacturing processes yield slightly different mechanical performance.
2) **Is there any obvious difference in mechanical performance depending on the layer orientation?**
   No, the layer orientation itself does not seem to affect the mechanical performance. However, the alignment of the prior β-grains which is connected to the layer orientation might change the mechanical performance.
3) **Is there any inhomogeneous strain fields that can be connected to the microstructure and building direction of additive manufactured Ti-6Al-4V?**
   Yes, strains are localized to individual grains or grain boundaries within the microstructure. The alignment of the prior β-grains could be critical for the strain fields arising.

5.1. Further recommendations

The authors would like to comment on things which would be of interest to further investigate. One of the major conclusions in this report is the behavior of mechanical performance depending on the growing direction of the prior β-grains. It would be interesting to study the fracture surface and see how the crack path is connected to these, and also to analyze the alloy composition around the crack. It would also be of interest to see how the growing direction of prior β-grains affects fatigue properties of components.

To draw further conclusions on how elongation at break varies between manufacturing processes and building direction, it would be of interest to investigate the severity and position of defects within samples.

It would also be of interest to investigate the tested samples and see if there are any strain hardening close to the fracture surface.

6. References

[1] G. Lütjering, J.C. Williams, Titanium, Berlin: Springer, 2007.

[2] S. Axelsson, "Surface Characterization of Titanium Powders with X-ray Photoelectron Spectroscopy," Department of Material and Manufacturing Technology, Chalmers University of Technology, Gothenburg, 2012.

[3] R. Pedersson, Microstructure and Phase Transformation of Ti-6Al-4V, Luleå: Luleå University of Technology, 2002.

[4] J. Karlsson, Optimization of Electron Beam Melting for Production of Small Components in Biocompatible Titanium Grades, Uppsala: Uppsala University, Applied Materials Sciences, 2015.

[5] E. Sallica-Levaa, A.L.Jardinib, J.B.Fogagnoloa,, "Microstructure and mechanical behavior of porous Ti–6Al–4V parts obtained by selective laser melting," *Journal of the mechanical behavior of biomedical materials,* vol. 26, pp. 98-108, 2013.

[6] B. Vayre, F. Vignat, F. Villeneuve, "Identification on some design key parameters for additive manufacturing: application on Electron Beam Melting," *Procedia CIRP,* vol. 7, p. 264 – 269, 2013.

[7] M.-D. Mohsen, Dictionary of Gems and Gemology, Springer-Verlag Telos, 2009.

[8] Edson Costa, Masanari Shiomi, Kozo Osakada, Tahar Laoui, "Rapid manufacturing of metal components by laser forming," *International Journal of Machine Tools & Manufacture,* vol. 46, pp. 1459-1468, 2006.

[9] Arcam AB, [Online]. Available: http://www.arcam.com/technology/electron-beam-melting/. [Accessed 05 02 2015].

[10] Lore Thijs, Frederik Verhaeghe, Tom Craeghs, Jan Van Humbeeck, Jean-Pierre Kruth, "A study of the microstructural evolution during selective laser melting of Ti–6Al–4V," *Acta Materialia ,* vol. 58, pp. 3303-3312, 2010.

[11] A. Safdar, L.-Y. Wei, A. Snis, Z. Lai, "Evaluation of microstructural development in electron beam melted Ti-6Al-4V," *Materials Characterization,* vol. 65, pp. 8-15, 2012.

[12] H.K. Rafi, N.V. Karthik, Haijun Gong, Thomas L. Starr, and Brent E. Stucker, "Microstructures and mechanical properties of Ti6Al4V parts fabricated by selective laser melting and electron beam melting," *Journal of Materials Engineering and Performance,* vol. 22, no. 12, pp. 3372-3383, 2013.

[13] Marlo Simonelli, Yau Yau Tse, C. Tuck, "The formation of alpha+beta microstructure in as-fabricated selective laser melting of Ti–6Al–4V," *Journal of Materials Research,* vol. 29, no. 17, pp. 2028-2035, 2014.

[14] L.E. Murr, E.V. Esquivel, S.A. Quinones, S.M. Gaytan, M.I. Lopez, E.Y. Martinez, F. Medina, D.H. Hernandez, E. Martinez, J.L. Martinez, S.W. Stafford, D.K. Brown, T. Hoppe, W. Meyersd, U. Lindhe, R.B. Wicker, "Microstructures and mechanical properties of electron beam-rapid manufactured Ti–6Al–4V biomedical prototypes compared to wrought Ti–6Al–4V," *Material Characterization,* vol. 60, pp. 96-105, 2009.

[15] M. Simonelli, Y.Y.Tse, C.Tuck, "Effect of the building orientation on the mechanical properties and fracture modes of SLM Ti-6Al-4V," *Materials Science & Engineering A,* vol. 616, p. 1–11, 2014.

[16] A. Safdar, H.Z. He, Liu-Ying Wei, A. Snis, Luis E. Chavez de Paz, " Effect of process parameters settings and thickness on surface roughness of EBM produced Ti-6Al-4V," *Rapid Prototyping Journal,* vol. 18, no. 5, pp. 401-408, 2012.

[17] Denis Cormier, Ola Harrysson, Jason Low, Kyle Knowlson, "Optimization of the Electron Beam Melting Process," in *IIE Annual Conference, Proceedings: 1*, Raleigh, 2004.

[18] Afshin Mohammadhosseini, S.H. Masood, Darren Fraser, Mahnaz Jahedi, "Mechanical Properties Investigation of HIP and As-Built EBM Parts," *Advanced Materials Research,* vol. 576, pp. 216-219, 2012.

[19] Marc André Meyers, Krishan Kumar Chawla, Mechanical Behavior of Materials : Second Edition, Cambridge: Cambridge University Press, 2009.

[20] Shih-Heng Tung, Ming-HsiangShih, Jui-ChaoKuo, "Application of High Magnification Digital Image Correlation Technique to Micromechanical Strain Analysis," *Optics and Lasersin Engineering,* no. 48, pp. 636-641, 2010.

[21] Jennifer L.W. Carter, Michael D. Uchic, Michael J. Mills, "Impact of speckle pattern parameters on DIC strain resolution calculated from in-situ SEM experiments," in *Fracture, Fatigue, Failure, and Damage Evolution, Volume 5*, Greenville, SC,, Springer Link, 2014.

[22] Joakim Karlsson, Torsten Sjögren, Anders Snis, Håkan Engqvist, Jukka Lausmaa, "Digital image correlation analysis of localstrain fields on Ti6Al4V manufactured by electron beam melting," *Materials Science&Engineering A,* vol. 618, p. 456–461, 2014.

[23] Marco Simonelli, Yau Tse, Christopher Tuck, "Microstructure and Mechanical properties of TI-6Al-4V Fabricated by Selective Laser Melting," *Supplemental Proceedings: Materials Processing and Interfaces TMS,* vol. 1, pp. 863-870, 2012.

[24] MARCO SIMONELLI, YAU YAU TSE, CHRIS TUCK, "On the Texture Formation of Selective Laser Melted Ti-6Al-4V," *METALLURGICAL AND MATERIALS TRANSACTIONS A,* vol. 45A, pp. 2863-2872, 2014.

[25] M.Simonelli, Y.Y. Tse, C. Tuck, "Further Understanding of Ti6Al4V Selective Laser Melting Using Texture Analysis.","* Proceedings of 23rd Annual International Solid Freeform Fabrication Symposium,* pp. 480-491, 2012.

7. Appendices

7.1. Appendix 1 - Mechanical data

EBM-X-AB	Sample 1	Sample 2	Sample 3	Sample 4	Mean	Std
Young's modulus [GPa]	112	110	112	111	111.1	0.92
Ultimate Tensile Strength [MPa]	959	956	958	951	955.9	3.20
Yield Strength (Rp0.2) [MPa]	847	847	846	845	846.2	0.87
Elongation at break [%]	20.2	19.1	20.3	18.5	19.5	0.87

EBM-Z-AB	Sample 1	Sample 2	Sample 3	Mean	Std
Young's modulus [GPa]	113	125	114	117.8	6.55
Ultimate Tensile Strength [MPa]	1012	1040	999	1017.1	21.04
Yield Strength (Rp0.2) [MPa]	918	959	914	930.4	24.78
Elongation at break [%]	14,6	6,7	12,5	11.3	4.10

SLM-X-AB	Sample 1	Sample 2	Sample 3	Mean	Std
Young's modulus [GPa]	105	109	109	107.5	2.39
Ultimate Tensile Strength [MPa]	1194	1215	1214	1207.8	11.89
Yield Strength (Rp0.2) [MPa]	1031	1055	1048	1044.9	12.50
Elongation at break [%]	8.3	10.1	10.6	9.6	1.21

SLM-Z-AB	Sample 1	Sample 2	Sample 3	Mean	Std
Young's modulus [GPa]	117	117	114	116.0	1.45
Ultimate Tensile Strength [MPa]	1249	1240	1228	1239.4	10.55
Yield Strength (Rp0,02) [MPa]	1147	1135	1130	1137.3	8.78
Elongation at break [%]	14,6	14,4	16,7	15.3	1.26

SLM-X-HT	Sample 1	Sample 2	Sample 3	Mean	Std
Young's modulus [GPa]	115	108	108	110.4	4.27
Ultimate Tensile Strength [MPa]	1135	1128	1112	1125.2	11.73
Yield Strength (Rp0,02) [MPa]	1053	1033	1015	1033,8	19.18
Elongation at break [%]	14,7	17,7	13,1	15.2	2.36

SLM-Z-HT	Sample 1	Sample 2	Sample 3	Mean	Std
Young's modulus [GPa]	112	113	113	112.4	0.70
Ultimate Tensile Strength [MPa]	1135	1143	1138	1138.5	3.86
Yield Strength (Rp0,02) [MPa]	1037	1065	1065	1055.5	16.08
Elongation at break [%]	15.7	16.3	16.0	16.0	0.32

7.2. Appendix 2 - Stress-strain curves

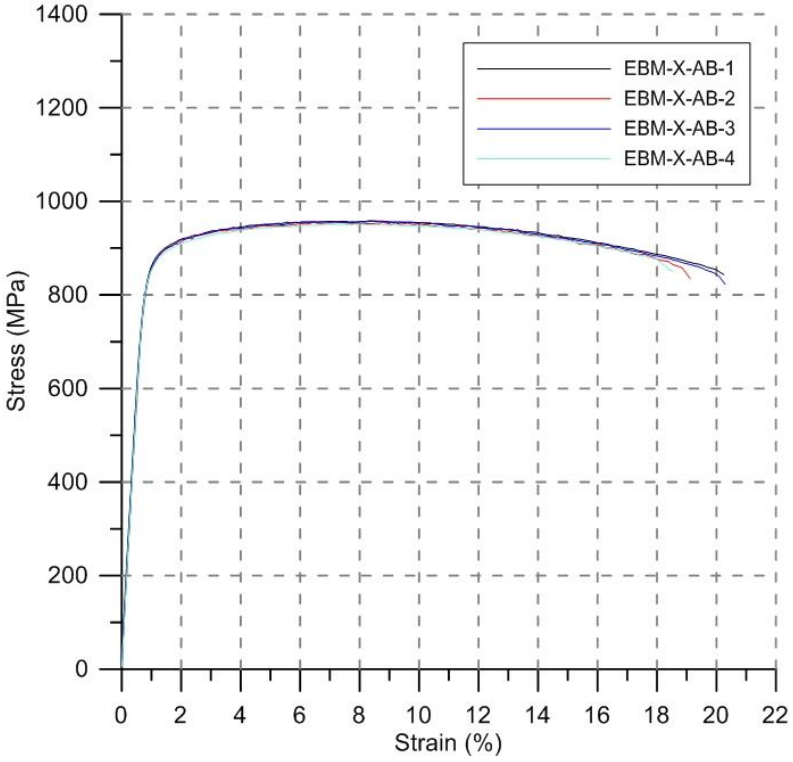

EBM-X-AB

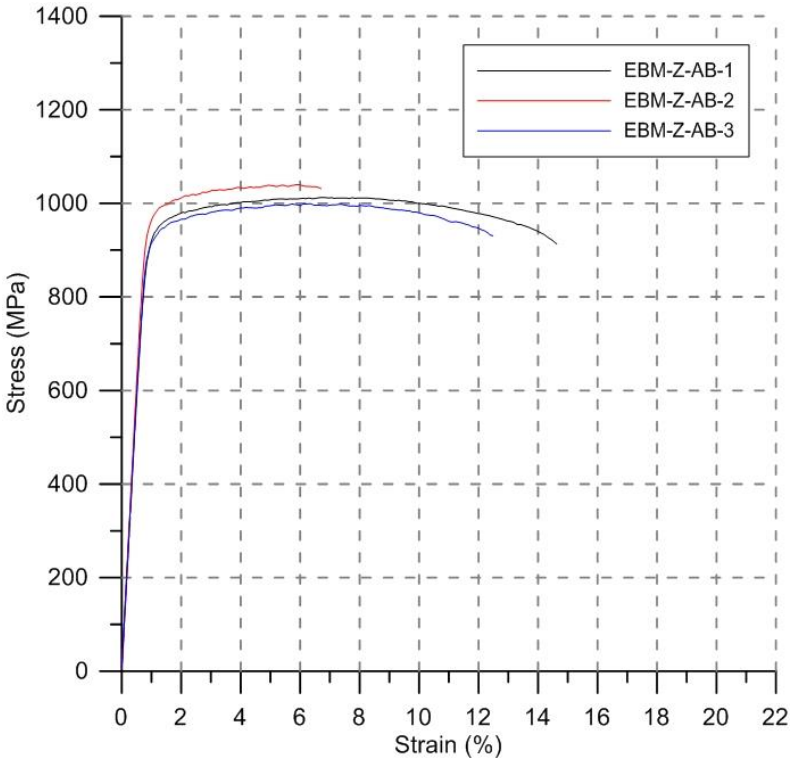

EBM-Z-AB

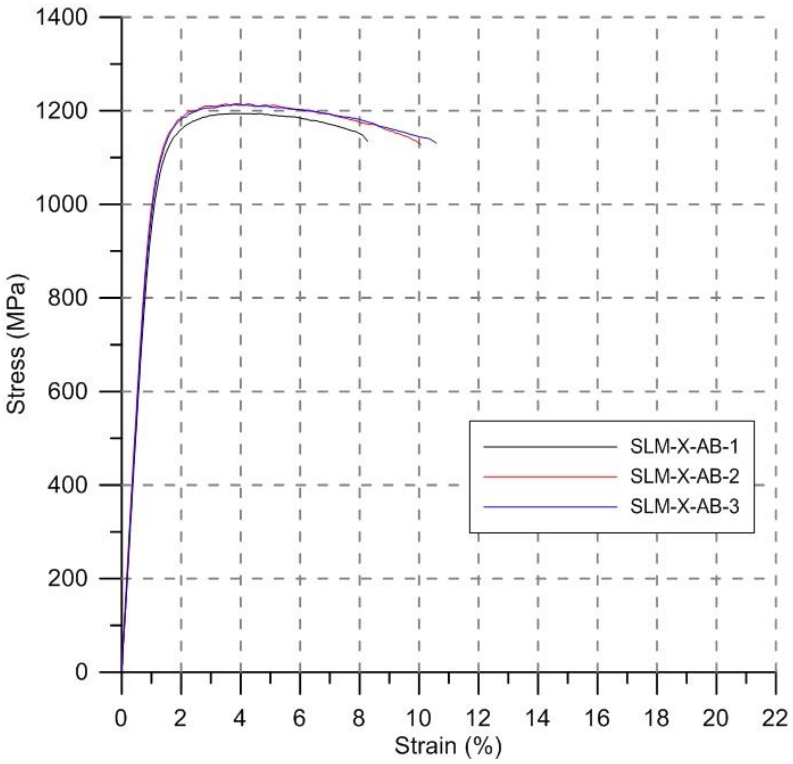

SLM-X-AB

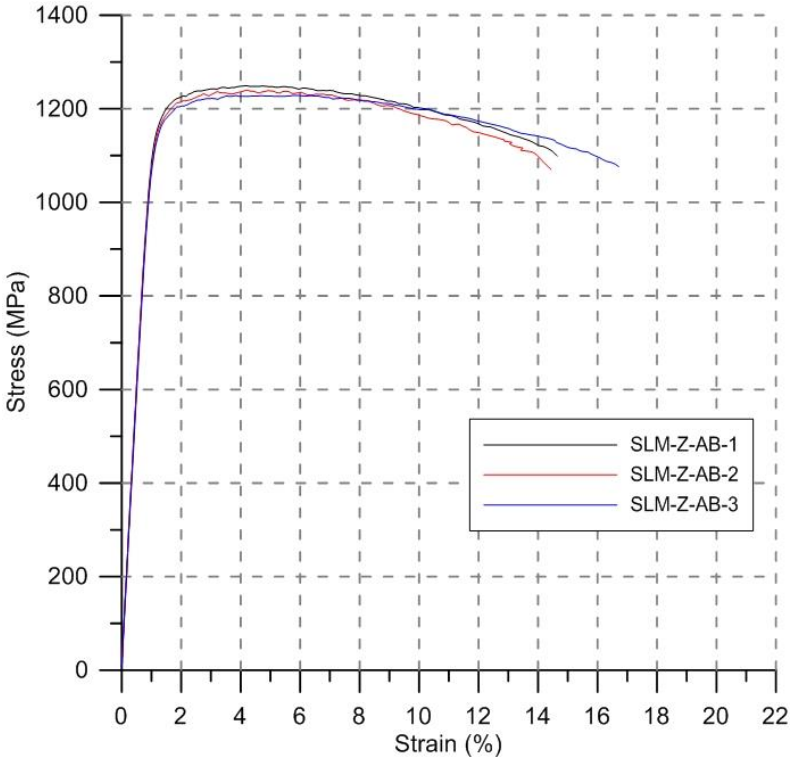

SLM-Z-AB

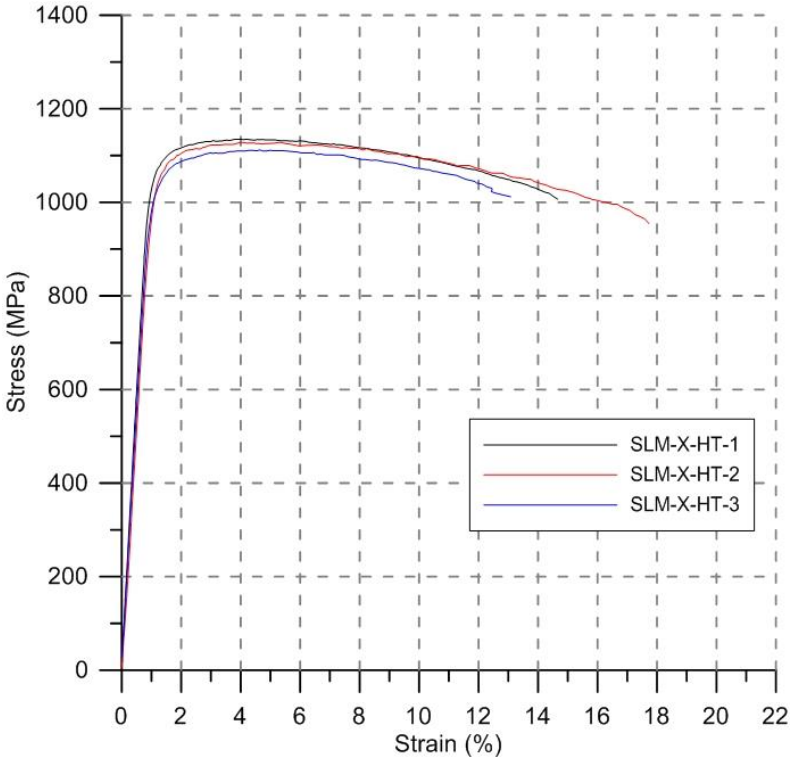

SLM-X-HT

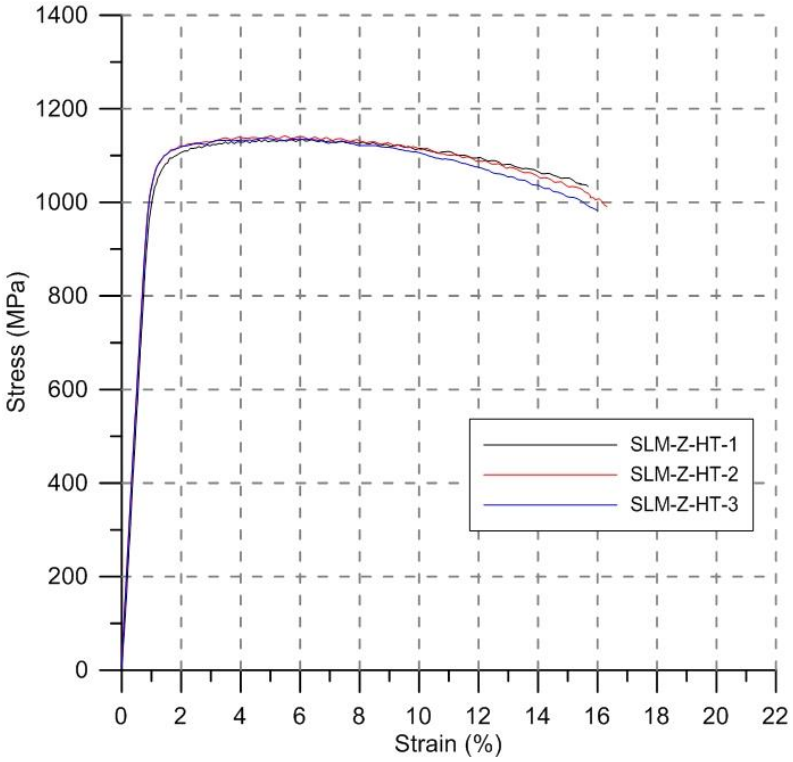

SLM-Z-HT